2006

Interfacial Temperatures at MEMS Switch Contact Asperities

Jiang Zhu
Western University

Interfacial Temperatures at MEMS Switch Contact Asperities

(Spine Title: Interfacial Temperatures at MEMS Switch Contact Asperities)

(Thesis Format: Monograph)

by

Jiang Zhu

Graduate Program in Engineering Science
Department of Mechanical and Materials Engineering

A thesis submitted in partial fulfillment
of the requirements for the degree of
Master of Engineering Science

Faculty of Graduate Studies
The University of Western Ontario
London, Ontario, Canada

CERTIFICATE OF EXAMINATION

THE UNIVERSITY OF WESTERN ONTARIO
FACULTY OF GRADUATE STUDIES

Chief Advisor

Prof. John Dryden

Examining Board

Prof. Douglas Shinozaki

Prof. Xueliang Sun

Prof. Serguei Primak

The thesis by
Jiang Zhu

entitled
Interfacial Temperatures at MEMS Switch Contact Asperities

is accepted in partial fulfillment of the
requirements for the degree of
Master of Engineering Science

Date Aug. 24, 2006

Prof. Jun Yang

Chairman of Examining Board

Abstract

This thesis covers a theoretical study of interfacial temperature generated at MEMS switch contact interfaces. A characterization of metal surface topography based on fractal geometry is presented. A surface model, a surface contact model and electrical contact resistance are discussed in the thesis. Further, a theoretical treatment of the general problem of electrical contact and heating is presented and developed. The interfacial temperature generated at micro electrical contact is analyzed and discussed, and the reason for the collapse of gold contact system before melting point of gold is given. Moreover, the interfacial temperature and contact heating analysis related to MEMS switch contact interfaces are discussed.

Acknowledgements

I would like to acknowledge my appreciation to the many people who assisted this thesis:

I would like to thank my advisors, Dr. John Dryden and Dr. Lior Kogut, for their supervision throughout this project. Their guidance and technical advice are greatly appreciated.

I would like to express many thanks to Dr. Z. Kucerovsky and Dr. X.A. Sun for their advice and generous help.

I also appreciate the assistance and help of my colleagues and friends Ms. R. Li, Mr. T. Wang, Mr. J. Lou and Mr. Y. Liu.

I also owe special thanks to my wife Xin Wang, my son Eric Honglin Zhu, whose continuous moral support made this thesis possible.

Contents

List of Tables

List of Figures

Nomenclature

L	sample length, Lorenz constant, gold wire length
G	fractal roughness
D	fractal dimension
M	the number of superposed ridges
L_s	cutoff length(smallest wavelength)
n	a frequency index
E	Young's modulus
E^*	effective elastic modulus
r, a_0	the real contact radius of a micro-contact spot
a	the real contact area of a micro-contact spot
r'	the truncated contact radius of a micro-contact spot
a'	the truncated contact area of a micro-contact spot
a'_s	smallest micro-contact area
a'_L	biggest micro-contact area
A	total real contact area, area of gold wire
A'	total truncated contact area
d_s	the diameter of the smallest truncated area
N_s	the number of surface points above the truncation plane
p_m	mean contact pressure of a micro-contact spot
P	total contact load
P_*	dimensionless contact load
A_*	dimensionless real contact area
N	the number of truncated asperities
l	electron mean free path length
R_M	Maxwell spreading resistance
R_S	Sharvin resistance
R_c	constriction resistance
R_C	total electrical contact resistance
R_0	constriction resistance at room temperature
k	thermal conductivity

k_0	thermal conductivity at room temperature
T	absolute temperature
T_0	room temperature
V, V_1, V_2	potentials
S, S_1, S_2	surfaces
U	applied voltage
I	current
$\vec{j}$	current density
U_*	dimensionless voltage
I_*	dimensionless current

Greek Symbols

α	the temperature coefficient of electrical resistivity
β	the temperature coefficient of thermal conductivity
γ	a scaling Parameter
$\phi_{m,n}$	a random phase
ν	Poisson's ratio
δ	local interference distance
Δ	surface interference distance
Δ_s	smallest surface interference distance
Δ_L	largest surface interference distance
ρ	electrical resistivity
ρ_0	electrical resistivity at room temperature
σ	electrical conductivity
σ_0	electrical conductivity at room temperature
σ_Y	yield strength
θ	supertemperature
θ_m	maximum supertemperature
$\theta_{m,*}$	dimensionless maximum supertemperature
ψ, ψ_0, $\psi_{m,n}$, Ω	transform functions

Chapter 1

Introduction

In view of the increasing number of Micro-Electro-Mechanical systems (MEMS) involving surface contact, understanding of the behavior of MEMS contact interfaces is imperative. Touch-mode MEMS devices are advantageous in many applications, such as electrostatic actuators, microswitches, and microrelays . The performance and lifetime of such microdevices depend on the behavior of their contact interfaces [1].

A Micro-Electro-Mechanical System (MEMS) is a batch-fabricated (micro-fabricated) system that contains both electrical and mechanical components with characteristic sizes ranging from nanometers to millimeters.

Initially MEMS techniques were borrowed directly from the integrated circuit (IC) fabrication technologies, hence, MEMS technology also holds many advantages of IC technologies. A few of the advantages include very low cost attributed to batch fabrication, tremendous size, weight and power reduction, and simultaneous great performance improvement [2, 3].

The development and application of MEMS and NEMS (Nano-Electro-Mechanical System) are critical to the current world as they will lead to major

breakthroughs in information technology, computers, medicine, health, manufacturing, transportation, energy, avionics, security, etc. Nowadays developing tendencies in engineering science have increased the importance on integrated synthesis, analysis, design and control of advanced MEMS and NEMS [4].

MEMS applications and markets begin where traditional IC applications and markets end. Commercially successful devices and systems that apply MEMS technologies include many micro- or nano-scale sensors (e.g., inertial sensors, pressure sensors, chemical sensors, etc.), actuators (e.g., micromirrors, micro-relays, micro-switches, micro-valves, etc.), and other Microsystems [2]. Today, MEMS are mostly found in automotive industry, but the devices have already extended to biomedical, computer, wireless and optical communication systems, military and other industrial areas.

With the recent progress of MEMS technology, the development of MEMS devices for radio frequency (RF) applications has been growing rapidly. RF MEMS devices have a broad range of potential applications in wireless communication, space, military, instrumentation, etc. RF MEMS switches are one of the most promising surface-micro-machined devices that have attracted many research efforts in recent years. Compared with conventional switches such as PIN diode or FET switches, RF MEMS switches show many advantages in terms of near-zero power consumption, very high isolation and linearity, low insertion loss, etc [5, 6]. Also, RF MEMS switches can be applied in broad areas because of their frequencies from RF to millimeter-wave (0.1 to 100GHz), such as Radar Systems for Defense Applications (5-94 GHz), Automotive Radars: 24, 60, and 77 GHz, Satellite Communication Systems (12-35 GHz), and Wireless Communication Systems (0.8-6 GHz) [6].

Two typical MEMS switches are shown in Figure 1.1. Figure 1.1 (*a*) [7] is the Analog devices MEMS-series inline switch developed in Northeastern

University Boston USA. Figure 1.1 (*b*) [8] is miniature inline-series switch (dc-contact) developed in MIT Lincoln Lab. Both of them are vertical metal contact switches. The contact material of the first device is gold while platinum-to-platinum contact is used by second one.

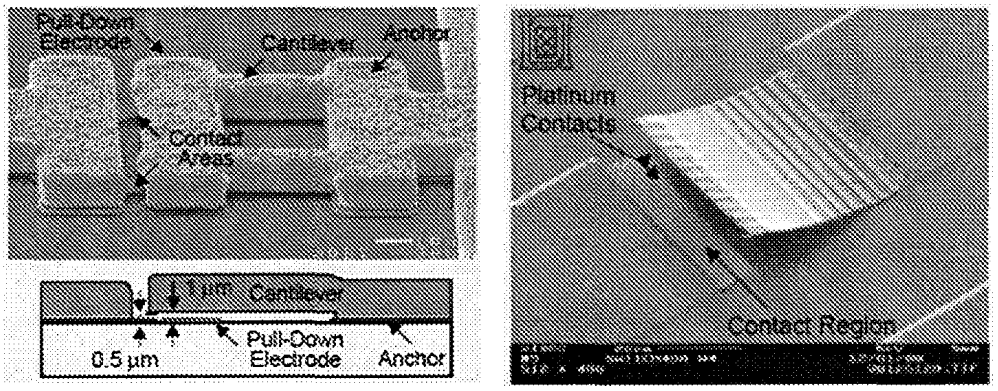

Figure 1.1: (*a*) Analog devices MEMS-series switch [7] (*b*) SEM of the dc-contact switch [8]

From their actuation mechanisms RF MEMS switches can be divided into electrostatic, magnetic, thermal, and piezoelectric types. Currently Most of researches focus on the electrostatic types because of its spectacular RF performance [6]. From their contact mechanisms two types of RF MEMS switches can be divided - metal contacting and capacitive coupling. MEMS Metal contacting switches has a broader frequency coverage than capacitive coupling switches which are not suitable for low frequency applications because of the capacitance nature. However, the contact lifetime of capacitive coupling switches is obviously longer than that of the metal contacting switches [3]. In addition, RF MEMS switches can be cataloged into series and shunt switches in terms of applications. Most metal contacting switches are often used as serial switches while the capacitive coupling switches are used for shunt switches. In this thesis we mainly focus on a metal contacting serial RF MEMS switch.

Even though RF MEMS switches have many advantages over traditional switches, there are still some problems need to be solved in the future, such as relatively Low Speed, Power Handling (lower than 100mW), High-Voltage Drive (reliable operation at 20-80V), Reliability (lower than 10 billion cycles), Packaging, and Cost, etc. [6].

Currently, the main failure analysis issue for RF MEMS metal contacting switches focuses on contact metallurgy [9]. However, understanding of contact properties and surface interactions at micron scale is challenging. Some of the failure mechanisms include adhesion, thermal softening, melting, micro-welding, material transfer, and increased contact resistance, etc. [10, 11, 12]. All of them are related to contact properties and metallurgy. The contact properties include surface topography [13] of contact interfaces, contact mechanics [14], electrical contact resistance [1], etc. In addition, the surface interactions due to deformation, current flow, heat generation affect the failure mechanisms significantly.

1.1 Surface Topography

Since the contact mechanism and metallurgy of MEMS switches are crucial to their failure mechanisms analysis and the surface topography is known to substantially affect the properties of contact materials, the surface topography of contact interfaces should play a significant role in these studies.

The real contacts between two rough surfaces occur only over highest asperities of the two surfaces. The total real contact area of the micro- contacts is typically a small fraction of apparent contact area [15, 16]. Greenwood and Williamson made the pioneering contribution for representing the topography of engineering surfaces by developing a popular elastic model (GW model).

In this model, two rough surfaces were represented by assuming them as a flat surface in normal contact with an equivalent rough surface. Also, it was assumed that the asperity heights follow a Gaussian distribution function, while all the radii of the asperities are same [15]. However, the values of the statistical parameters used in this model, such as the height variance, slope, and curvature of surface asperities the dependence on the statistical parameters depend on sample size and revolution of measuring instrument. To get objective contact mechanism analysis of contact rough surfaces, these shortcomings of GW model can be solved by using scale-independent parameters to characterize surface topography [13, 17].

In view of the random and multi-scale properties of surface topography, fractal geometry [18], pioneered by Benoit Mandelbrot, has been used recently to study rough surfaces. Due to the inherent advantages of fractal geometry, such as scale-independence (independence of sample size effects and resolution of measuring instrument) and self-affinity [13, 17], it avoids the shortcomings of GW model and characterizes the surface topography well. The researches in references [13, 14] generated a three-dimensional fractal surface topography by a modified (truncated) two-variable Weierstrass-Mandelbrot function. The simulated 1μm $\times$ 1μm isotropic fractal surface is shown in Figure 1.2. This surface model will be analyzed in detail in the following contact analysis. One of the earliest studies to use fractal geometry for surface topography is that of reference [19]. It was shown that small asperities deform plastically while large asperities deform elastically which is a totally different result from what is predicted from the GW model. Researchers of reference [13] introduced the fractal contact model prescribed above based on a modified three-dimensional W-M function for elastic-plastic surface in normal contact and obtained numerical results for the average contact pressure and real contact area in terms of the

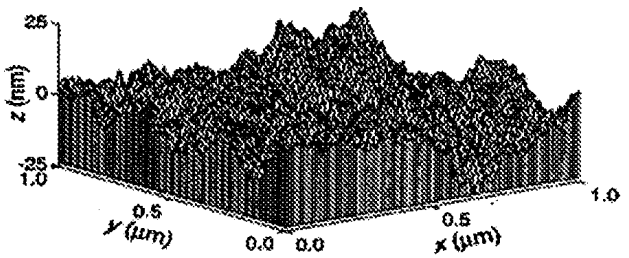

Figure 1.2: A simulated fractal surface $1\mu m \times 1\mu m$ [13]

mean surface separation distance. However, in their study, the stress-strain behavior of asperities was assumed to be either purely elastic or fully plastic, i.e., the intermediate range of elastic-plastic deformation was not considered.

In order to obtain relations between the mean contact pressure and real contact area for a single spherical asperity indenting an elastic-plastic homogeneous medium a finite element model was developed [14] which characterized a single asperity micro-contact and interactions occurring at multi-scale contact interfaces of layered media based on fractal surface topography. In this model the elastic-plastic deformation was considered and the stress-strain constitutive relation and the real contact area corresponding to the purely elastic, fully plastic, and elastic-plastic deformation regimes were characterized in details.

There are two main assumptions in this so-called elastic-plastic constitutive model. First, a system of two contacting rough surfaces was replaced by an equivalent system of a rigid rough surface and a flat deformable surface with an effective elastic modulus. Second, even though there are numerous spherical asperity micro-contacts in the contact interface, it is assumed that they are enough far away from each other and the asperity interactions could be neglected. This is a reasonable assumption since the real contact area is much smaller than apparent contact area and interference distance is small.

Figure 1.3 is a schematic of a micro-contact between an upper rigid spherical rough surface and a flat deformable surface. Here, r is real contact radius of the real contact area a , r' is the truncated contact radius of the truncated contact area a' and δ is local interference distance.

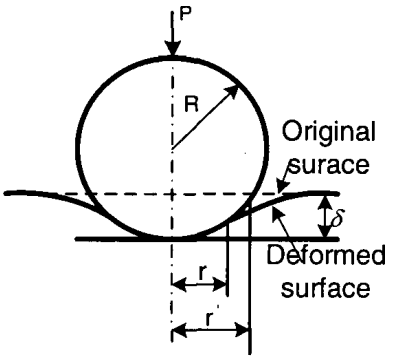

Figure 1.3: Schematic of a micro-contact between an upper rigid spherical rough surface and a flat deformable surface (reproduced from [20])

1.2 Electrical Contact Resistance

The electrical contact resistance (ECR) of rough surfaces is significantly important in many fields of science and engineering [1], especially in MEMS. For example, the operation and lifetime of some MEMS devices, such as micro-switches, micro-relays and connectors, greatly depend on the ECR performance.

The ECR at a single micro-contact is attributed to the constriction resistance R_c , which arises due to the convergence and divergence of the electrical current flow through the micro-contact during switch closure [16]. When the contact radius r is much larger than the electron mean free path length l of

the material ($r \gg l$), the constriction resistance is dominated by a scattering or diffusive mechanism, given by the Maxwell spreading resistance [1, 16].

On the other hand, when the radius r is smaller than the electron mean free path length l ($r \ll l$), the constriction resistance is dominated by the Sharvin mechanism, in which electrons travel through the micro-contact ballistically without undergoing any scattering [21]. Figure 1.4 is the schematic illustration of diffusive (left) and ballistic (right) electron transport in a micro-contact. In

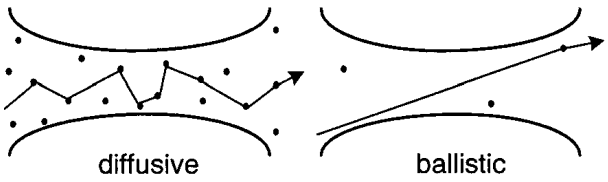

Figure 1.4: Schematic of diffusive (left) and ballistic (right) mechanism (reproduced from [22])

the intermediate range, neither Sharvin mechanism nor Maxwell spreading is in dominance. To a quite good approximation, the constriction resistance is described by Wexler's interpolation formula [23] which will be discussed further in Chapter 3.

For most MEMS devices, due to relatively light contact loads, the ratio of real contact area and apparent contact area is between 10^{-4} and 10^{-2} . Such small micro-contacts lead to the predominance of Sharvin mechanism in the ECR [1].

1.3 The Temperature-Voltage Relation of Theoretical Electrical Contact Theory

As mentioned above, surfaces of metals are rough no matter how carefully they are prepared. The nature of the contact between two metals is markedly influenced by the roughness of the two contact surfaces. When two metals are brought into contact, just highest asperities of the surfaces contact each other. The real contact area is just a small fraction of the apparent contact area (10^{-4} to 10^{-2}) [15, 16].

If there is a current flow between the contact metals, the current flow must pass the metal micro-contact through those highest asperities, converging then diverging. The constriction resistance causes the Joule heating in the micro-contact and the temperature in the micro-contact is much higher than the surrounding bulk metal. [16, 24, 25]. The heat generation in the micro-contact often causes thermal softening, melting, micro-welding, etc., and decreases the reliability and life of devices. Therefore, it is important to understand contact temperature for the study, design and use of contacts. Figure 1.5 indicates the molten gold has splashed from micro-contact interfaces onto the surrounding cold metal, where it has frozen.

One method to determine the temperature of a micro-contact is to use the theoretical temperature-voltage relation [16, 26] which indicates the relation between the applied voltage across the micro-contact and maximum temperature in contact interface. By utilizing this relation, we can calculate maximum temperature in contact interface from applied contact voltage. Further, a new mathematical treatment of the general problem of electrical heating had been presented in [24, 26]. The researchers in [24] investigated the interface temper-

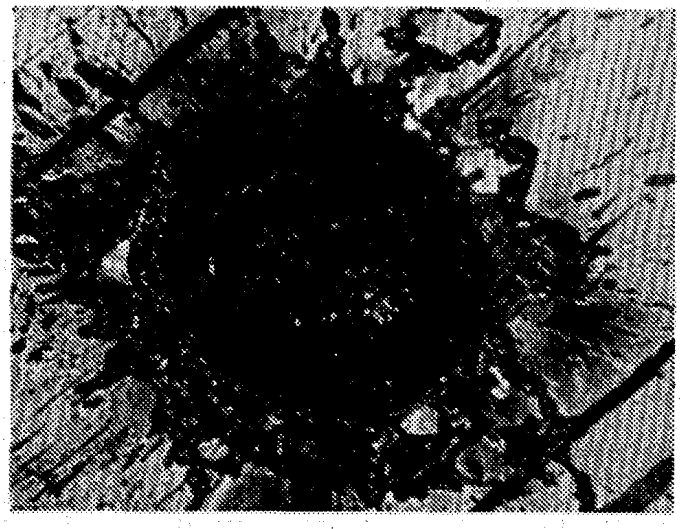

Figure 1.5: Photomicrograph of a gold surface showing the damage caused in region of contact by the passage of a high current. Magnification ×120. [24]

ature between the contact of two gold bulks due to the passage of an electric current from a high impedance source [27] and heat generated in the constricted region of the contact interface. They observed the collapse of the contact system occured at the temperature calculated from the temperature-voltage relation around 950 °C which is lower than the melting point of gold (1064 °C). Further, the metallographic evidence showed clearly that some of the gold had reached the melting point, 1064 °C. Later on, the researchers in [26] suggested that at high temperatures the behaviour of the contact region is not adequately described by the accepted theory. They developed a theoretical treatment of the general problem of electrical contact and heating. The relations they obtained include the relation between the temperature at any point and the maximum temperature, the relation between the total current and the maximum temperature and the relation between the current density at any point and the total current, etc. Also, they discussed the reason of the phenomena described in study [24]. In this thesis we developed

their theories and clearly revealed the reason of the phenomena described in study [24] in Chapter 4.

Both of the thermal conductivities and the electrical resistivities of metals are temperature dependent. The thermal conductivity of gold decreases when temperature increases [28]. The electrical resistivity of gold varies obviously with temperature and increases when temperature increases [29]. This makes the problem more complicated, however, the thermal conductivities and the electrical resistivities of metals follow the Wiedemann-Franz Law [16] which indicates the relation among the thermal conductivity, the electrical resistivity and the temperatures.

1.4 Thesis Outline

The general approach of this study aims at finding out what will happen in the interfaces of a micro-switch or a micro-relay when electric currents pass through the interfaces. During contact, some portions of the interfaces will melt and weld because of high temperature. Sometimes the molten gold might be splashed from the surfaces. When the molten metal solidifies, the two surfaces may bond and the device will damage and fail. Even though there is no melting or splashing, high temperature may change mechanical properties of the material of the micro-relay, soften the asperities of the surfaces and make larger real contact area and larger adhesion, which also will lead to the failure of the device.

The objectives of this study include:

1. Study metal surface topography, contact model and electrical contact resistance in micro scale;

2. Solve the temperature field across contacting surfaces of a micro-switch subject to electric current flow;

3. Study the effect of elevated temperatures at micro-switch interfaces on the mechanical response (thermal softening), real contact area, adhesion, and permanent failure of the micro-switch due to micro-welding.

Figure 1.6 shows schematically how the various parameters are interconnected. The fractal surface analysis is based on a 1μm $\times$ 1μm gold sample, and the effects of related material properties, fractal roughness G, and fractal dimension D, to the surface topography are discussed. Then, a contact model due to applied load P is described and related material properties include Young's modulus E, Poisson's ratio ν and yield strength σ_Y. Since the real contact area a_i of the i^{th} asperity is obtained, the electrical contact resistance can be calculated and the material electrical resistivity ρ, electron mean free path l are applied here. Further, the temperature and heat transfer in contact interfaces are analyzed and discussed, the related material property is thermal conductivity k. The maximum temperature T_{mi} of the i^{th} asperity in contact interfaces is computed. When it is higher than the melting point of gold micro-welding will happen. The device will damage and fail. When T_{mi} is less than the melting point, material softening and adhesion will change the contact mechanics of the device such as the real contact area and electrical contact resistance of the material. This might lead to the failure of the device.

Conclusions based upon existing data and theoretical computations are included in the last chapter.

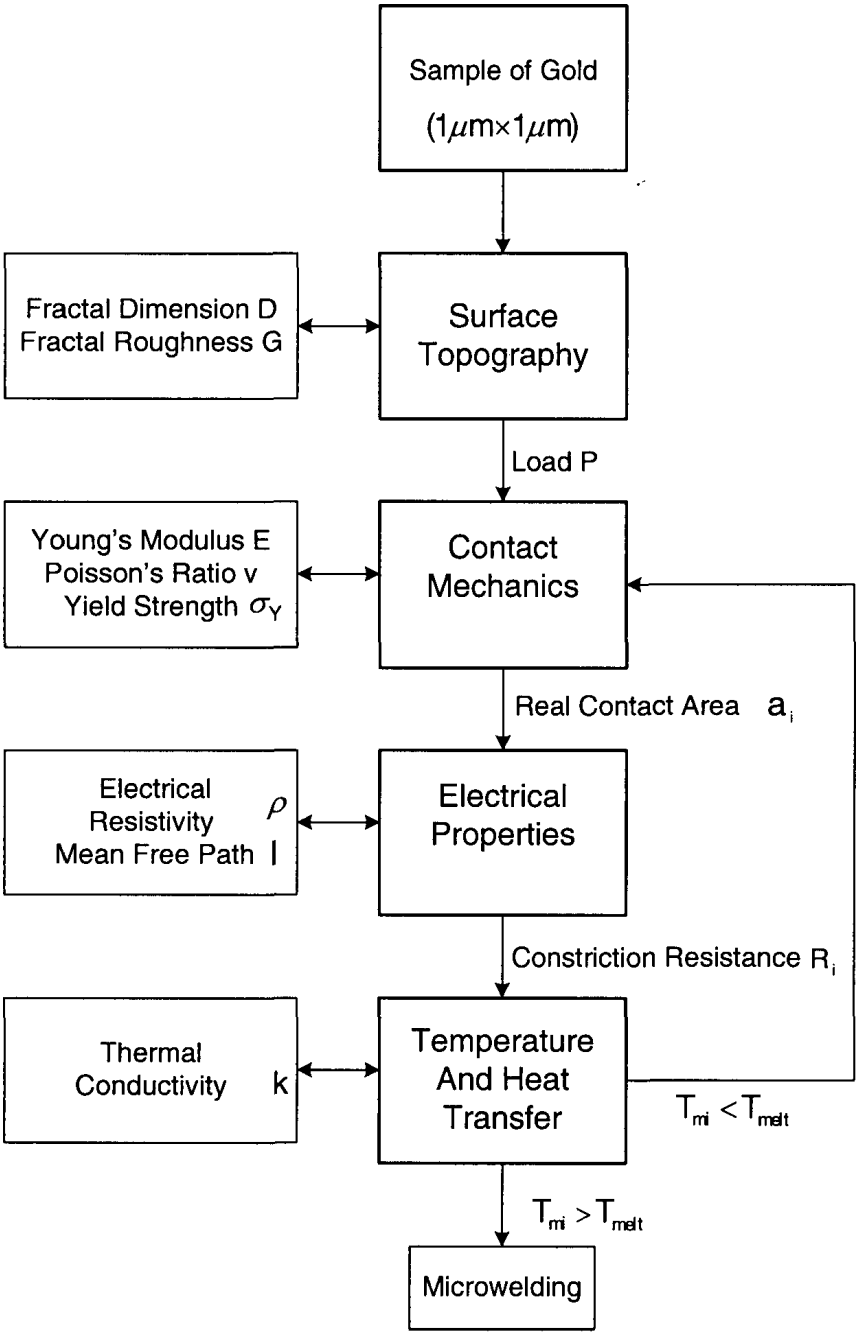

Figure 1.6: Flow chart

Chapter 2

Contact Modeling

As mentioned in Chapter 1, the main failure analysis focuses on the contact properties and metallurgy for MEMS metal contacting switches [9]. The contact properties mainly include surface topography of contact interfaces and contact mechanics. In this chapter we will explore them and study how the related material properties affect them.

2.1 Fractal Surface Characterization

Many conventional analytical approaches for surface topography are based on the Greenwood–Williamson (GW) model [15]. However, this model is scale-dependent, the values of the statistical parameters used in this model, such as the height variance, slope, and curvature of surface asperities depend on sample size and revolution of measuring instrument. In order to account for the effect of surface topography that is random and multi-scaled, it is necessary to use a scale-independent model. A fractal approach essentially serves the purpose. The concept of fractal geometry pioneered by Benoit Mandelbrot [18] has been

used recently to characterize rough surfaces and contact problems.

2.1.1 The Fractal Surface Model

In this thesis we use the modified (truncated) two-variable Weierstrass-Mandelbrot function mentioned before to generate a three-dimensional fractal surface topography [13].

$$z(x,y) = L\left(\frac{G}{L}\right)^{(D-2)}\left(\frac{\ln\gamma}{M}\right)^{1/2}\sum_{m=1}^{M}\sum_{n=0}^{n_{max}}\gamma^{(D-3)n}(\cos\phi_{m,n} - \cos\psi_{m,n}), \quad (2.1)$$

where,

$$\psi_{m,n} = \frac{2\pi\gamma^n(x^2+y^2)^{1/2}}{L}\cos\left[\tan^{-1}\left(\frac{y}{x}\right) - \frac{\pi m}{M}\right] + \phi_{m,n}.$$

Here, L is the sample length, G is the fractal roughness, D is the fractal dimension of the surface ($2 < D < 3$), $\gamma(\gamma > 1)$ is a scaling parameter, M is the number of superposed ridges used to construct the surfaces, n is a frequency index, with $n_{max} = \text{int}[\log(\text{L}/\text{L}_\text{s})/\log\gamma]$ representing the upper limit of n , where L_s is the cut-off length (smallest length between two points), and $\phi_{m,n}$ is a random phase. The chosen material is $1\mu\text{m} \times 1\mu\text{m}$ gold sample so the sample length $L = 1\mu\text{m}$. The scaling parameter γ controls the density of frequencies in the surface profile. Considering surface flatness and frequency distribution density, γ is chosen to be 1.5 [13]. The cut-off length L_s is set to equal to 1nm. The ridge number M is chosen to be 10. The fractal roughness G is a height scaling parameter independent of frequency. The magnitude of the fractal dimension D determines the contribution of high and low frequency components in the equation. Thus, larger values of D indicate that higher

frequency components are more dominant than lower frequency components in the surface topography profile. In this equation the only unknown variables are G and D , which can be determined experimentally.

2.1.2 Generation of the Surface

First, we divided each side of the sample by 1000, so the total points on the surface is one million. Then, we wrote a Fortran programme (see appendix A) to calculate the height $z(x, y)$ of each point. In this programme, we use SUBROUTINE QUICK SORT to sort the values of $z(x, y)$ in a sequence from the lowest one to the highest one. The function of the CALL RANDOM NUMBER(R) is to obtain a random number for each loop of the function "$z(x, y)$" , since there is a random phase $\phi_{m,n}$ in the equation (2.1). Therefore, each time we run the same programme we will get a different surface even though we do not change anything in the programme.

After running the programme in Fortran, we use the obtained data to generate the rough surface in Matlab.

2.1.3 Effects of Fractal Parameters G and D

Before the analysis of effects of G And D , we first elucidate the effects of L_s and M to the surface topography.

The cut-off length L_s represents the smallest wavelength. For fixed G, D and M , when $L_s = 1\mu$m which is the sample length L, it means there is just one wave in x direction (Fig. 2.1 (a)). Comparing with Figure 2.1 (b) where $L_s = 1$nm , we can see the obvious difference between them. In both of them $M = 1$, it means there is one superposed ridge, so we can see there is just a straight line in y direction. However, when the ridge number $M = 3$, it is

not a straight line any more in y direction and a visually random surface is obtained (Fig. 2.2 (b)).

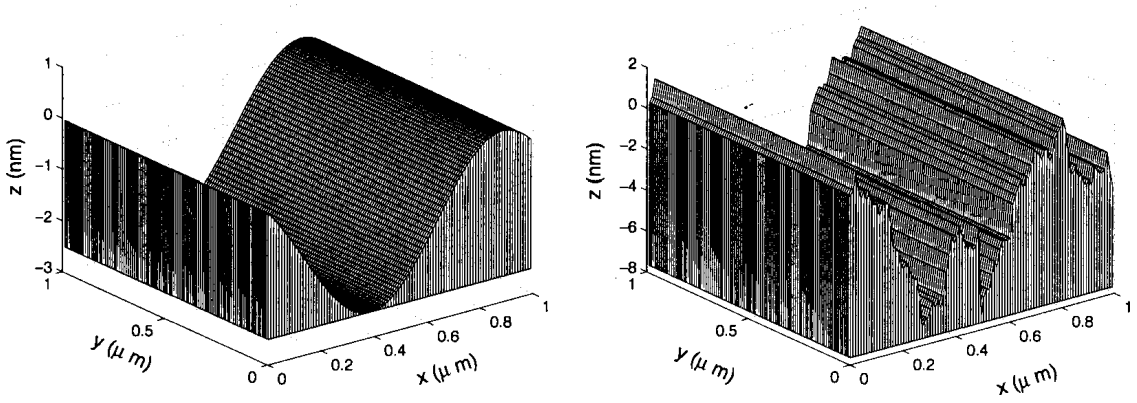

(a) $L_s = 1\mu$m (b) $L_s = 1$nm

Figure 2.1: Simulated three-dimensional fractal surfaces ($D = 2.44$, $G = 9.46 \times 10^{-13}$m, $M = 1$)

To illustrate the physical significance of the fractal parameters G And D on the surface topography, another two pairs of simulated fractal surfaces are shown in Figure 2.3 (a)-(b) and Figure 2.4 (a)-(b). The fractal roughness G is a height scaling parameter independent of frequency. The comparison of Figure 2.3 (a) and (b) indicate that the bigger G value yields the rougher surface topography. This is expected since G affects the amplitude term in equation (2.1). However, for fractal dimension D , the situation is reverse. Even though the magnitude of the fractal dimension D determines the contribution of high- and low-frequency components in equation (2.1) and high D values indicate the dominance of high-frequency components in the surface topography, increasing D value yields a smoother topography (Fig. 2.4 (a)-(b)).

Comparing Figure 2.3 (b) with Figure 2.4 (b), we gain the evidence that even though both of them have same parameters ($D = 2.44$, $G = 9.46 \times$

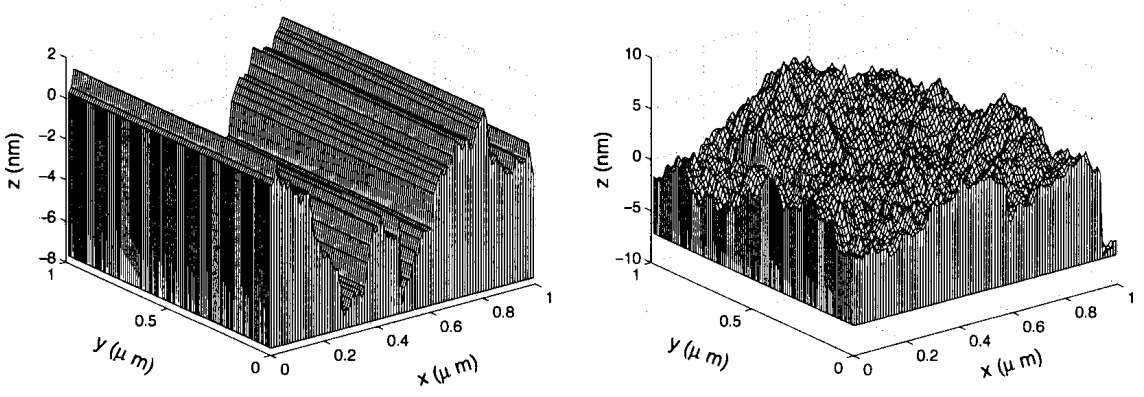

(a) $M = 1$ (b) $M = 3$

Figure 2.2: Simulated three-dimensional fractal surfaces ($D = 2.44$, $G = 9.46 \times 10^{-13}$m, $L_s = 1$nm)

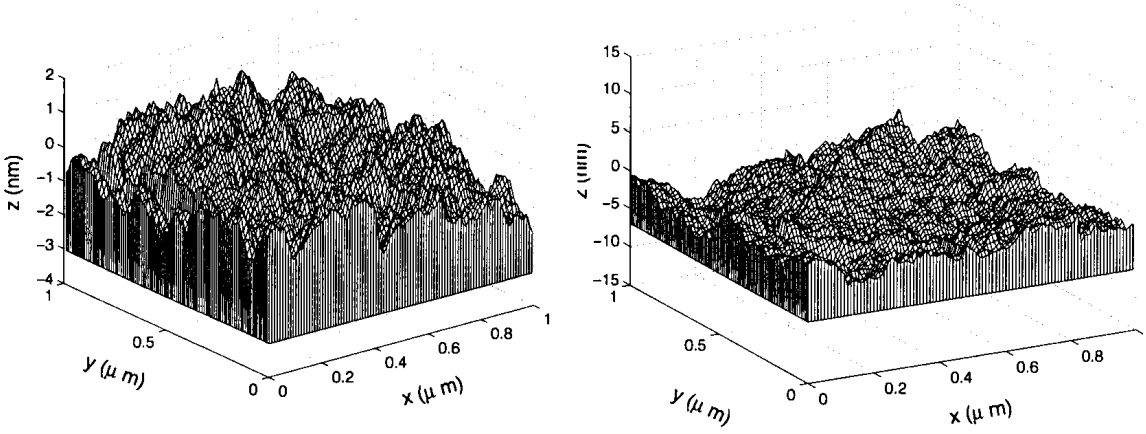

(a) $G = 9.46 \times 10^{-14}$m (b) $G = 9.46 \times 10^{-13}$m

Figure 2.3: Simulated three-dimensional fractal surfaces ($D = 2.44$, $L_s = 1$nm, $M = 10$)

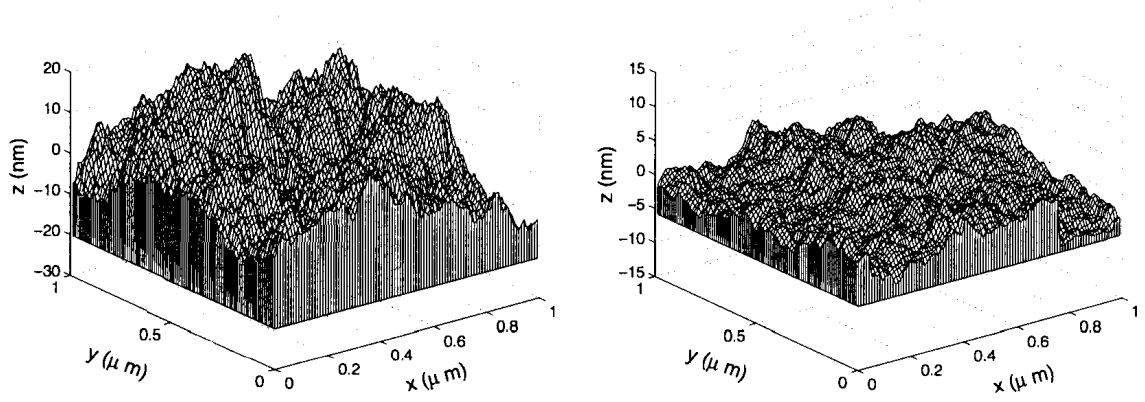

(a) $D = 2.34$ (b) $D = 2.44$

Figure 2.4: Simulated three-dimensional fractal surfaces ($G = 9.46 \times 10^{-13}$m, $L_s = 1$nm, $M = 10$)

10^{-13}m, $M = 10$, $L_s = 1$nm), the surface topographies are different for running the programme two times due to the existence of the random phase in the equation (2.1). However, since their fractal roughness and dimension are same, there should have some similarities between their mechanical properties. We will discuss it in next section.

2.2 Contact Mechanics Analysis

2.2.1 Elastic-Plastic Deformation Model

Figure 2.5 (left) could be utilized to simulate two MEMS switch contact interfaces which are closing together. The interfaces are not perfectly smooth due to the surface roughness and topography. When the two interfaces are closing, just the highest asperities come into contact. Therefore, the surface contact comprises numerous asperity micro-contacts which are assumed as spherical in shape. Another assumption is the micro-contacts are apart from each other

sufficiently and the asperity interactions among them can be neglected. This is a reasonable approximation for relatively light contact loads where the real contact area A is a small percentage of the apparent contact area A_a [16]. The system of these two contacting rough surfaces can be represented by an equivalent system of a flat deformable surface with a rigid rough surface (Fig 2.5 (right)). Here, the material Young's moduli can be transferred to an effective elastic modulus E^*

$$\frac{1}{E^*} = \frac{1-\nu_1^2}{E_1} + \frac{1-\nu_2^2}{E_2}, \tag{2.2}$$

where ν_1 , ν_2 , and E_1 , E_2 , are the Poisson's ratios and elastic moduli of the two interacting surfaces, respectively. Here, gold Young's modulus $E = 80 \times 10^9$Pa and Poisson's radio $\nu = 0.44$ [30]. Based on these assumptions and the knowledge of the mean contact pressure at asperity micro-contacts and real micro-contact area, the total contact load and total real contact area can be obtained using an integration procedure [14].

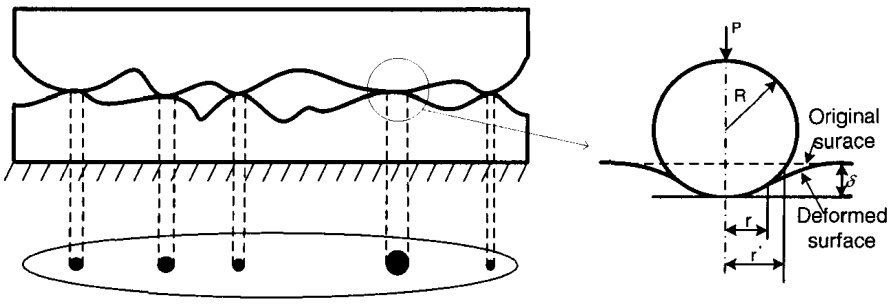

Figure 2.5: Contacting rough surfaces

In the study of [14], the stress-strain behavior was divided into three kinds of deformations-purely elastic, elastic-plastic and fully plastic deformation, depending on the values of the representative strain, $E^*\delta/\sigma_Y r'$, where δ is the

interference distance between the rigid sphere and the surface of the deformable medium, σ_Y is the yield strength of the deformable medium and r' is the radius of the truncated contact area a' , the mean contact pressure, p_m , and the real contact area, a , were obtained due to the interference distance δ . A constitutive elastic-plastic deformation model for a single asperity micro-contact was generated as [14],

For elastic deformation ($E^*\delta/\sigma_Y r' < 1.78$),

$$\frac{p_m}{\sigma_Y} = \frac{4\sqrt{2}}{3\pi}\left(\frac{E^*\delta}{\sigma_Y r'}\right), \quad \frac{a'}{a} = 2. \tag{2.3}$$

For elastic-plastic deformation ($1.78 \leq E^*\delta/\sigma_Y r' < 21$),

$$\begin{aligned} \frac{p_m}{\sigma_Y} &= 0.70\ln\left(\frac{E^*\delta}{\sigma_Y r'}\right) + 0.66, \\ \frac{a'}{a} &= 0.05\left[\ln\left(\frac{E^*\delta}{\sigma_Y r'}\right)\right]^2 - 0.57\ln\left(\frac{E^*\delta}{\sigma_Y r'}\right) + 2.41. \end{aligned} \tag{2.4}$$

For fully plastic deformation ($21 \leq E^*\delta/\sigma_Y r' \leq 400$),

$$\frac{p_m}{\sigma_Y} = 2.9, \quad \frac{a'}{a} = 0.05\left[\ln\left(\frac{E^*\delta}{\sigma_Y r'}\right)\right]^2 - 0.57\ln\left(\frac{E^*\delta}{\sigma_Y r'}\right) + 2.41. \tag{2.5}$$

For fully plastic deformation ($400 \leq E^*\delta/\sigma_Y r'$),

$$\frac{p_m}{\sigma_Y} = 2.9, \quad \frac{a'}{a} = 0.71. \tag{2.6}$$

This elastic-plastic deformation model reflects a continuous transition from elastic to fully plastic deformation. For any contact asperity in the regime, its mean contact pressure, p_m , and real contact area, a , can be found out, depending on its representative strain, $E^*\delta/\sigma_Y r'$, and truncated contact area

a' . Then, by using an integration procedure the total contact load and total real contact area can be obtained, which will be discussed in the following subsection.

2.2.2 Surface Contact Model

As mentioned above, the equivalent contact model of two rough surfaces comprises a rigid spherical rough surface and a deformable flat medium. The mechanical properties of the medium and the surface topography (described by fractal geometry) of the rough surface are equivalent with those of real contacting surfaces. The total contact load and total real contact area at a given surface interference distance can be obtained if we find out the values of the local surface interference distance and the truncated radius of each micro-contact asperity.

To find out the truncated radius of the i^{th} micro-contact asperity, r_i' , we need to get the value of the total truncated area A' first. Following an analytical procedure similar to the studies [13, 14], A' is given by

$$A' = \int_{a_s'}^{a_L'} a' n(a') da', \tag{2.7}$$

where a' is the truncated area of a single micro-contact, a_L' and a_s' are the largest and smallest truncated micro-contact areas, respectively, and $n(a')$ is the truncated asperity size distribution function.

The number of truncated asperities, N, with areas greater than a particular truncated area, a' , is assumed to follow the power-law relation [18],

$$N(a') = \left(\frac{a_L'}{a'}\right)^{(D-1)/2}. \tag{2.8}$$

Eventually, the total number of truncated asperities, at a given surface interference distance Δ , can be expressed as

$$N(a'_s) = \left(\frac{a'_L}{a'_s}\right)^{(D-1)/2} . \tag{2.9}$$

For a continuum, the size of the smallest micro-contact asperity should be bigger than the atomic dimensions, therefore, the diameter d_s of the smallest truncated area, a'_s , is assumed to be six times the lattice dimension of the contact material [14]. In this study, we set $d_s = 1\text{nm}$.

At a given surface interference distance Δ , the number of micro-contact asperities with their truncated areas between a' and $a' + da'$ is $n(a')da'$. So, the truncated asperity size distribution function can be calculated by [13]

$$n(a') = -\frac{dN(a')}{da'} = \frac{(D-1)}{2} {a'_L}^{(D-1)/2} {a'}^{(D+1)/2} . \tag{2.10}$$

Substituting equation (2.10) into equation (2.7), the total truncated area of the fractal surface can be written as [14]

$$A' = \frac{D-1}{3-D}\left(a'_L - {a'_L}^{(D-1)/2} {a'_s}^{(3-D)/2}\right) . \tag{2.11}$$

At a given surface interference Δ , the total truncated contact area, A' , can be obtained by numerical integration. The number of surface points N_s above the truncation plane was determined and the ratio of the total truncated area and the apparent area ($A_a = 10^{-12}\text{m}$) equals to the ratio of the number of truncated surface points to the total number of points ($1000 \times 1000 = 10^6$).

See equation below

$$\frac{A'}{A_a} = \frac{N_s}{10^6}.$$

For relatively light contact loads the total real contact area of the micro-contacts is typically a small fraction of apparent contact area (between 10^{-4} to 10^{-2}) [15, 16]. We preset the smallest total truncated area and biggest total truncated area as 10^{-4} and 10^{-2} of the apparent area , respectively, then the surface interferences are decided (see Figure 2.6). After this procedure, from the obtained total truncated area A' , the truncated area of the largest micro-contact, a'_L was calculated from equation (2.11). Then the total truncated asperities can be generated from equation (2.9). Also, the truncated area of i^{th}asperity a'_i was calculated using equation (2.8).

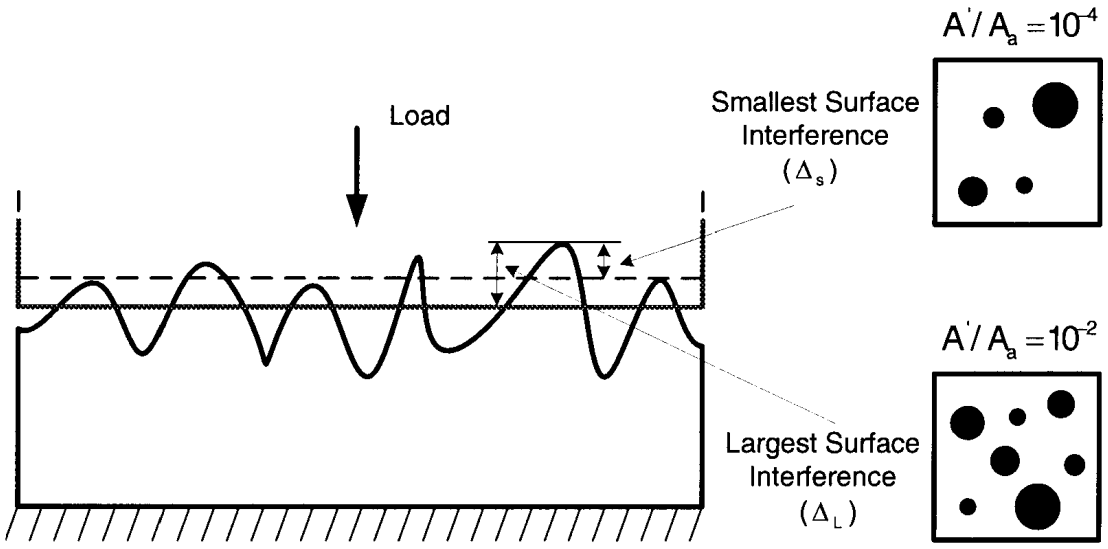

Figure 2.6: Schematic of contact surface interference

The i^{th} truncated asperity radius r'_i can be calculated from a'_i. The local

interference, δ_i , at the *ith* asperity is given by [13]

$$\delta_i = 2G^{(D-2)}(\ln\gamma)^{1/2}(2r_i')^{(3-D)}. \tag{2.12}$$

Then the representative strain $E^*\delta_i/\sigma_Y r_i'$ at the i^{th} asperity was obtained. Subsequently, from the elastic-elastic deformation model (Eqs. (2.3)-(2.6)), the mean contact pressure, $p_{m,i}$, and real contact area, a_i , at the i^{th} asperity micro-contact were determined. Finally, the total contact load, P, and total real contact area, A, were obtained by numerical integration,

$$P = \sum_{i=1}^{N(a_s')} p_{m,i}a_i, \tag{2.13}$$

and

$$A = \sum_{i=1}^{N(a_s')} a_i. \tag{2.14}$$

2.2.3 Results and Discussion

The chosen values of the parameters in the surface model (Eq. (2.1)) are shown in the Table 2.1

Table 2.1: Surface model parameters

Parameters	Values	Physical Meanings
L	1μm	Sample Length
G	9.46×10^{-13}m	Fractal Roughness
D	2.44	Fractal Dimension
γ	1.5	Scaling Parameter
M	10	Number of Superposed Ridges
L_s	1nm	cutoff length(smallest wavelength)

As mentioned previously, the surface topographies are different for running the programme two times due to the existence of the random phase in the equation (2.1). So, we just chose this surface topography for following surface contact calculation. Table 2.2 shows the calculation results of total truncated area, A', biggest truncated area, a'_L, total contact asperities and the ratio of a'_L and A', depending on different surface interference, Δ. It indicates that A', a'_L and total contact asperities all increase as the surface interference Δ increases, however, the ratio a'_L/A' decreases slowly, which is reasonable since there are more and more asperities contact each other. Nevertheless, biggest truncated area, a'_L is a big portion of total truncated area, A' (from 0.427 to 0.558). Therefore, the calculation of a'_L is critical for the analysis of surface contact.

Table 2.2: Surface model results

Δ[m]	A'[m^2]	a'_L[m^2]	Contact Asperities	Ratio of a'_L to A'
8.51E-10	1.00E-16	5.58E-17	21	5.58E-01
1.94E-09	1.00E-15	4.67E-16	99	4.67E-01
2.55E-09	2.00E-15	9.03E-16	159	4.52E-01
2.86E-09	3.00E-15	1.33E-15	211	4.44E-01
3.08E-09	4.00E-15	1.76E-15	258	4.40E-01
3.26E-09	5.00E-15	2.18E-15	301	4.36E-01
3.44E-09	6.00E-15	2.60E-15	342	4.34E-01
3.58E-09	7.00E-15	3.02E-15	381	4.32E-01
3.69E-09	8.00E-15	3.44E-15	418	4.30E-01
3.79E-09	9.00E-15	3.86E-15	454	4.29E-01
3.88E-09	1.00E-14	4.27E-15	489	4.27E-01

Figure 2.7 indicates the relation between biggest truncated area, a'_L and

surface interference, Δ. Figure 2.8 indicates the relation between the ratio, a'_L/A' and surface interference, Δ. In the calculations we set the diameter of the smallest truncated area, $d_s = 1\text{nm}$.

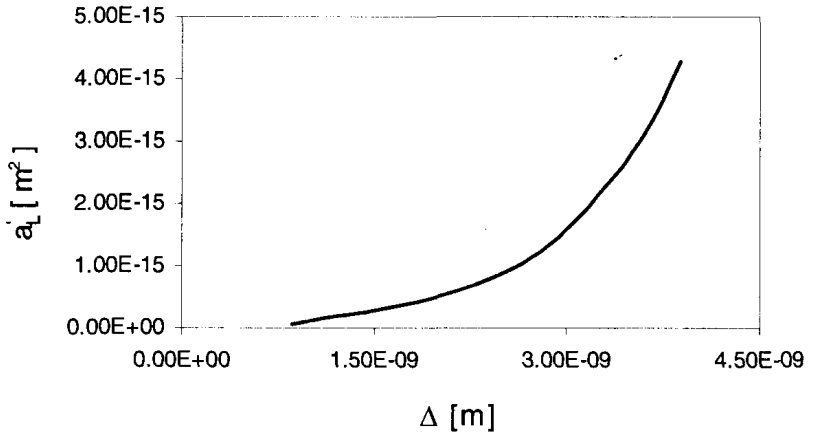

Figure 2.7: Biggest truncated area vs. surface interference

As mentioned previously, we need to use equation (2.2) to calculate the effective elastic modulus E^* of contact medium. Since we use two gold contact surfaces, the equation can be converted into

$$E^* = \frac{E}{2(1-\nu^2)},$$

where Young's modulus of gold $E = 80 \times 10^9\text{Pa}$ and Poisson's radio $\nu = 0.44$ [30]. The yield strength σ_Y is approximately equal to one third of the material hardness [14], in this study we chose $\sigma_Y = 0.53 \times 10^9\text{Pa}$.

The calculation results for total real contact area A and total contact load P are shown in Table 2.3. We use dimensionless contact load $P_* = P/A_a E^*$ which is total contact load P divided by apparent area A_a and the effective elastic modulus of gold E^* as x-axis and dimensionless real contact area $A_* = A/A_a$ which is total real contact area A divided by apparent area A_a as y-axis. The

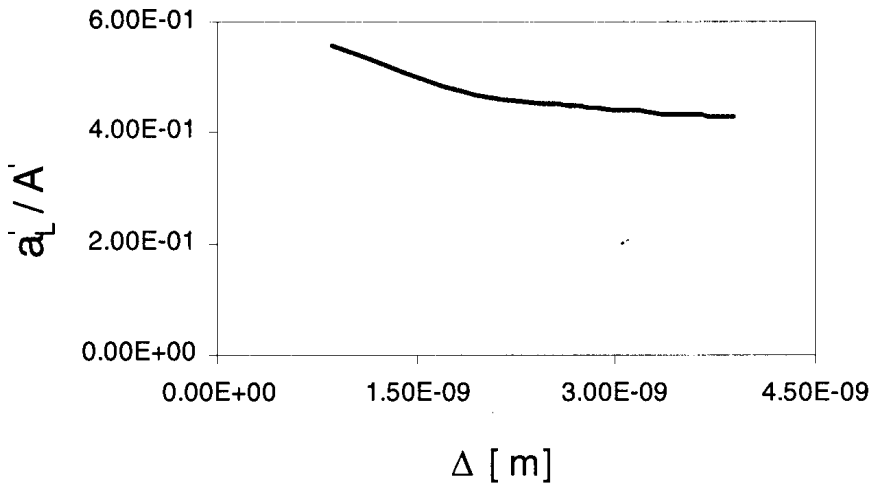

Figure 2.8: The ratio of biggest truncated area to total truncated area vs. surface interference

relation between contact load and real contact area is shown in Figure 2.9 which indicates the total real contact area increases approximately linearly as the total contact load increases.

The relation between the ratio of real contact area to apparent area (A_*) and surface interference is shown in the Figure 2.10 which indicates that the real contact area increases as the surface interference increases and the real contact area is just a very small fraction of the apparent contact area.

The significance of the fractal roughness G and the fractal dimension D on the total contact load and real contact area can be interpreted in light of the results shown in Figures 2.11 and 2.12 , respectively. For fixed contact load, decreasing the fractal roughness increases the real contact area significantly (Fig. 2.11). This is expected because G is a height scaling parameter, smaller G values correspond to smoother surface topographies, therefore, under same contact load, smoother surfaces result in larger real contact areas. A similar trend occurs when the fractal dimension D increases (Fig. 2.12). Since larger

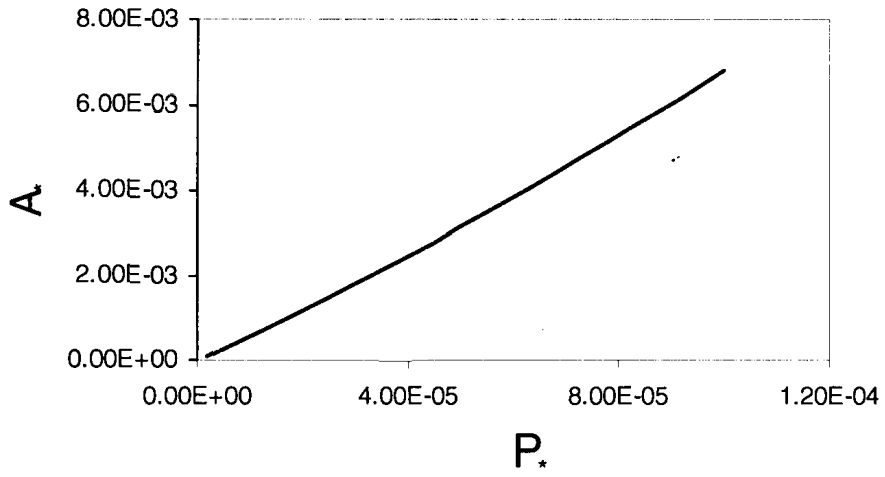

Figure 2.9: The relation between dimensionless contact load and dimensionless real contact area

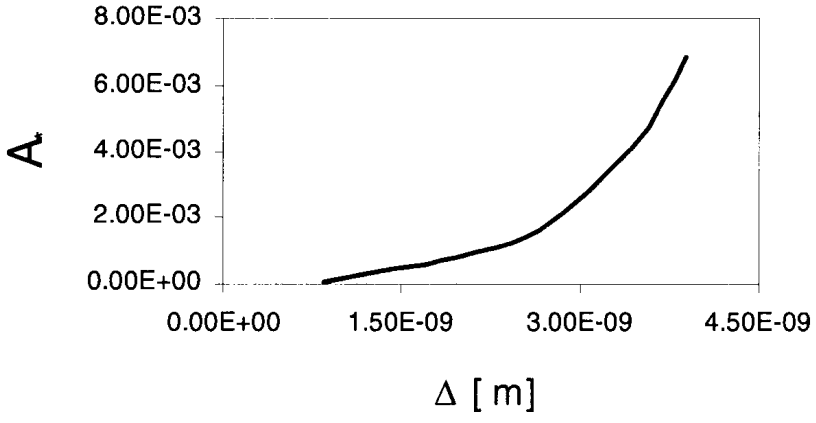

Figure 2.10: Dimensionless real contact area vs. surface interference

Table 2.3: Total real contact area and contact load

Δ[m]	A[m^2]	$P[N]$	A/A_a	P/A_aE^*
8.51E-10	8.55E-17	8.60E-08	8.55E-05	1.73E-06
1.94E-09	7.52E-16	6.63E-07	7.52E-04	1.34E-05
2.55E-09	1.45E-15	1.22E-06	1.45E-03	2.46E-05
2.86E-09	2.13E-15	1.74E-06	2.13E-03	3.50E-05
3.08E-09	2.81E-15	2.24E-06	2.81E-03	4.51E-05
3.26E-09	3.46E-15	2.71E-06	3.46E-03	5.47E-05
3.44E-09	4.12E-15	3.18E-06	4.12E-03	6.41E-05
3.58E-09	4.77E-15	3.64E-06	4.77E-03	7.33E-05
3.69E-09	5.50E-15	4.13E-06	5.50E-03	8.33E-05
3.79E-09	6.17E-15	4.58E-06	6.17E-03	9.22E-05
3.88E-09	6.82E-15	5.00E-06	6.82E-03	1.01E-04

D values are associated with smoother surface topographies, which, obviously, lead to larger real contact areas under same contact load.

In conclusion, a normal contact analysis of two rough gold surfaces characterized by three dimensional fractal geometry has been presented. Random rough surfaces were generated from the developed fractal model. The significance of the fractal roughness G and the fractal dimension D on the total contact load and real contact area were discussed in detail. The biggest truncated area, a'_L is a big portion of total truncated area, A'. Therefore, the calculation of a'_L is critical for the analysis of surface contact.

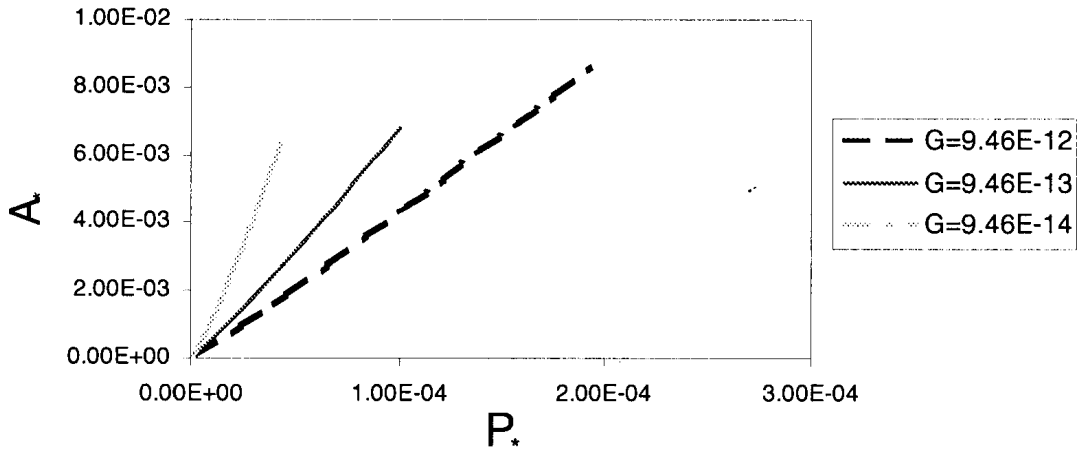

Figure 2.11: Effect of the fractal roughness G on the dimensionless total contact load and real contact area

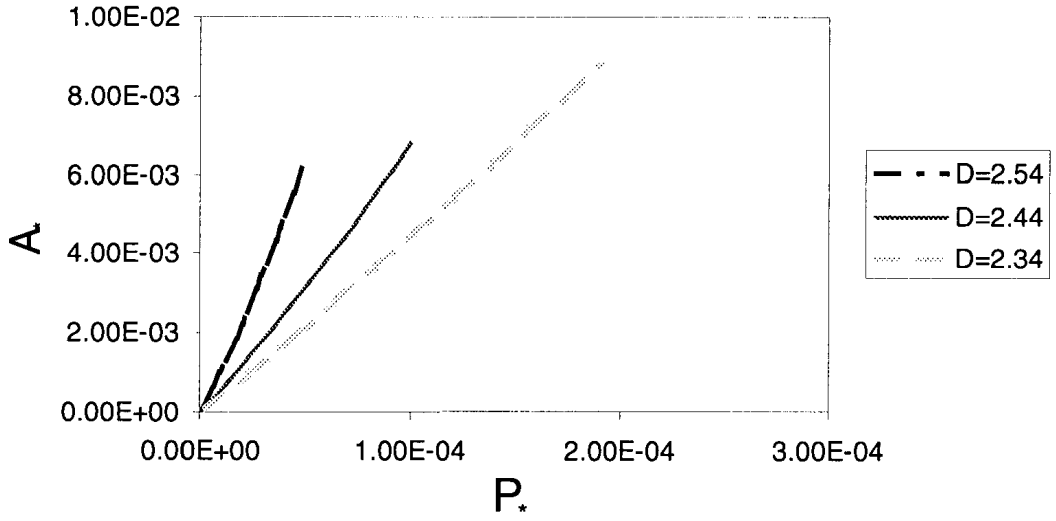

Figure 2.12: Effect of the fractal dimension D on the dimensionless total contact load and real contact area

Chapter 3

Electrical Contact Resistance Analysis

Electrical contact resistance (ECR) is caused by the roughness of contact surfaces. When two rough surfaces are pressed together, just highest asperities make contact. Therefore, the constriction resistance at each asperity is generated due to the convergence and divergence of the current flow passing through the micro-contact spot (Fig 3.1 and 3.2). Since all the constriction resistances are in parallel, the total electrical contact resistance

$$R_C = \left[\sum_{i=1}^{N(a_s')} R_{ci}^{-1} \right]^{-1}, \tag{3.1}$$

where R_{ci} is the constriction resistance at the i^{th} asperity. As mentioned in Chapter 1, the constriction resistance is composed by both of Maxwell spreading resistance and Sharvin resistance. When the contact radius a_0 is much larger than the electron mean free path length l of the material ($a_0 \gg l$), the constriction resistance is dominated by a scattering or diffusive mechanism,

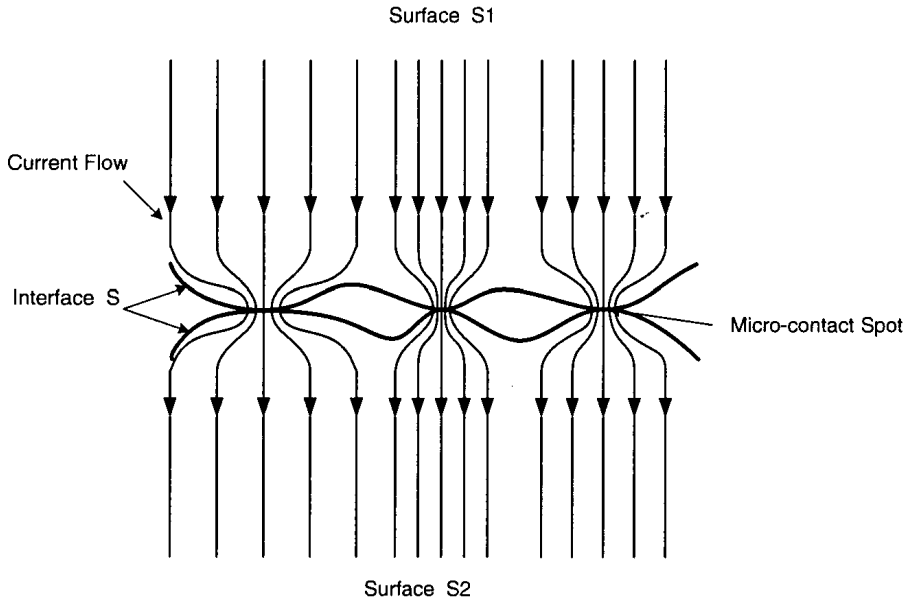

Figure 3.1: Schematic of current flow passing through electrical contact interfaces

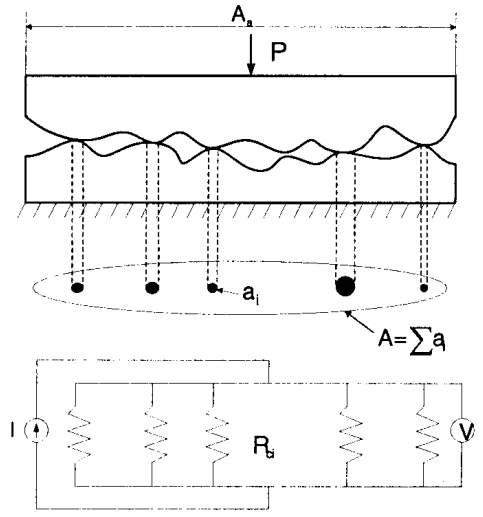

Figure 3.2: Schematic of MEMS contact interfaces (reproduced from [1])

given by the Maxwell spreading resistance [1, 16],

$$R_M = \frac{\rho}{2a_0} \,. \tag{3.2}$$

When the radius a_0 is smaller than the electron mean free path length l of the material ($a_0 \ll l$), the constriction resistance is dominated by Sharvin mechanism, in which electrons travel through the micro-contact ballistically without undergoing any scattering [21],

$$R_S = \frac{4\rho l}{3\pi {a_0}^2}, \tag{3.3}$$

where R_S is so-called Sharvin resistance. In the intermediate range, neither Sharvin mechanism nor Maxwell scattering Mechanism is in dominance. To a quite good approximation, the constriction resistance is described by Wexler's interpolation formula [23]

$$\begin{aligned} R_c &= \frac{4\rho l}{3\pi {a_0}^2} + \Gamma(K)\frac{\rho}{2a_0} \\ &= R_S + \Gamma(K) R_M, \end{aligned} \tag{3.4}$$

where $\Gamma(K)$ is a slowly varying function of the ratio $K = l/a_0$, with $\Gamma(0) = 1$ and $\Gamma(\infty) = 0.694$ (Fig. 3.3).

From Table 2.2 the biggest truncated area $a'_L = 4.27 \times 10^{-15}\mathrm{m}^2$ for largest surface interference $\Delta_L = 3.88 \times 10^{-9}\mathrm{m}$, so the radius of biggest micro-contact spot $a_0 = 36.8 \times 10^{-9}\mathrm{m}$. Since the electron mean free path of gold $l = 40\mathrm{nm}$ [30], all the micro-contact spots radii are smaller than the electron

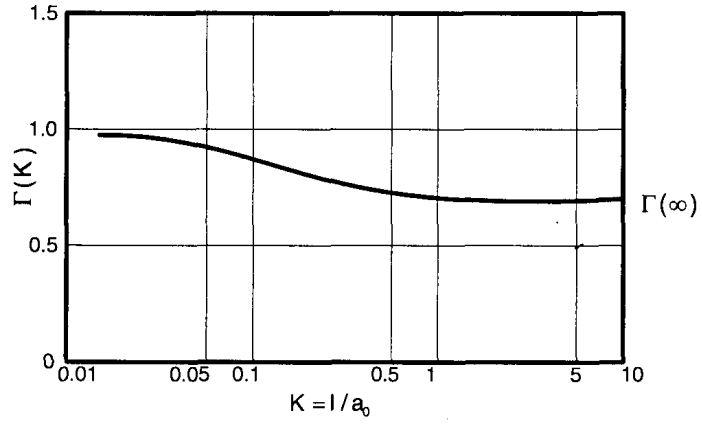

Figure 3.3: The slowly varying function $\Gamma(K)$ vs. $K = l/a_0$ (reproduced from [23])

mean free path of gold. We can assume $\Gamma(K) = 0.694$ and obtain

$$R_{ci} = \frac{4\rho l}{3\pi {a_{0,i}}^2} + 0.694\frac{\rho}{2a_{0,i}} \tag{3.5}$$

Table 3.1 shows the calculation results of total electrical contact resistance, $R_C[\Omega]$, total contact pressure $P/A_a[\mathrm{N/m^2}]$, depending on different surface interference, Δ. The logarithmic scale relation of electrical contact resistance and contact pressure is shown in Figure 3.4 which indicates that the electrical contact resistance decreases as the contact pressure increases. This is expected because the real contact area increases as the contact pressure increases.

To sum up, Electrical contact resistance (ECR) is caused by the roughness of contact surfaces. The constriction resistance of a particular contact asperity is composed of the Maxwell resistance or the Sharvin resistanceby or both of them, depending on ratio of the electron mean free path length, l, and the radius of the asperity, a_0.

However, the effect of the resistance described in equation (3.5) on the re-

lationship between voltage and contact temperature is not immediately apparent. Moreover, the relation between the electrical resistivity and the contact temperature is not shown in this equation. In real situation, due to the convergence and divergence of the current flow passing through the micro-contact spot, the contact temperature of the spot increases very quickly [16]. The electrical resistivity of the metal material varies obviously with temperature and increases when temperature increases [29]. In next chapter (Temperature Analysis), we focus on the effects of temperature at the micro-contact spot on the mechanical and electrical properties of contact medium. The relationships among maximum temperature, current flow and applied voltage are described.

Table 3.1: Electrical contact resistance and contact pressure

Δ[m]	P/A_a[N/m^2]	R_C[Ω]
8.51E-10	8.60E+04	1.49E+01
1.94E-09	6.63E+05	1.79E+00
2.55E-09	1.22E+06	9.51E-01
2.86E-09	1.74E+06	6.60E-01
3.08E-09	2.24E+06	5.08E-01
3.26E-09	2.71E+06	4.17E-01
3.44E-09	3.18E+06	3.54E-01
3.58E-09	3.64E+06	3.09E-01
3.69E-09	4.13E+06	2.72E-01
3.79E-09	4.58E+06	2.44E-01
3.88E-09	5.00E+06	2.23E-01

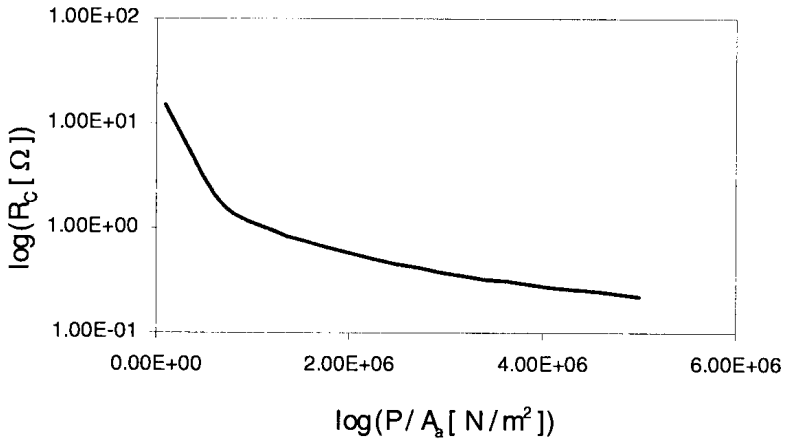

Figure 3.4: Logarithmic scale relation of electrical contact resistance vs. contact pressure

Chapter 4

Temperature Analysis

4.1 Temperature-Dependent Thermal Conductivity and Electrical Resistivity of Gold

4.1.1 The Thermal Conductivity

The magnitude of the thermal conductivity of a given metal depends on its microscopic structure and also tends to vary somewhat with temperature. The temperature dependence of thermal conductivity k[W/mK] of gold is shown in Table 4.1 [28]. It indicates that the thermal conductivity decreases when temperature increases but it varies very slowly. See Figure 4.1. At room

Table 4.1: Thermal conductivity of gold

Temperature T[K]	200	300	400	500	600	800	1000	1200
Thermal Conductivity k[W/mK]	323	317	311	304	298	284	270	255

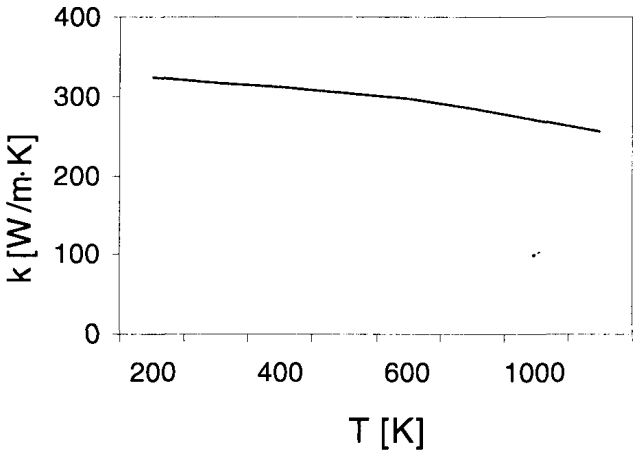

Figure 4.1: Temperature dependent thermal conductivity of gold

temperature, $T_0 = 298$K and thermal conductivity, $k_0 = 317$W/mK, we set $\theta = T - T_0$, where θ is supertemperature, T is absolute temperature, then,

$$k = k_0(1 - \beta\theta). \tag{4.1}$$

where, β is the temperature coefficient of the thermal conductivity and approximately equal to 2×10^{-4} for gold.

4.1.2 The Electrical Resistivity

The electrical resistivity of a metal varies with temperature and increases when temperature increases. It can also be represented by a linear function of temperature [29]

$$\rho = \rho_0(1 + \alpha\theta), \tag{4.2}$$

where α, the temperature coefficient of the electrical resistivity, is of the order of magnitude of 1/2 per cent for ordinary metal. ρ_0 is the resistivity at room temperature. If we choose $\rho_0 = 2.25510^{-8}\Omega$m as room temperature resistivity

where $T_0 = 298$K (see Table 4.2) [31], then α approximately equals to 4×10^{-3} which is much larger than the temperature coefficient of the thermal conductivity, $\beta = 2 \times 10^{-4}$. The curve of resistivity vs. temperature is almost linear (Fig 4.2).

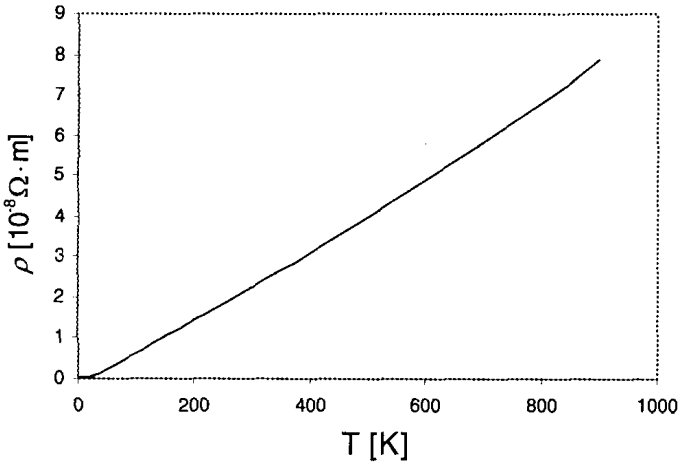

Figure 4.2: Temperature dependent electrical resistivity of gold

4.1.3 The Wiedemann-Franz Law

The Wiedemann-Franz Law [16] states that the thermal conductivity k and the electrical resistivity ρ obey the relation

$$k\rho = LT, \tag{4.3}$$

where L is Lorenz constant ($2.45 \times 10^{-8}(\mathrm{V/K})^2$). From this relation we can obtain $\frac{k\rho}{T} = \frac{k_0\rho_0}{T_0}$, then using $\theta = T - T_0$, it follows that

$$k\rho = k_0\rho_0 \left(1 + \frac{\theta}{T_0}\right). \tag{4.4}$$

Table 4.2: Electrical resistivity of gold

Temperature T[K]	Electrical Resistivity $\rho[10^{-8}\Omega m]$
1	0.022
10	0.0226
20	0.035
40	0.141
60	0.308
80	0.481
100	0.65
150	1.061
200	1.462
273	2.051
293	2.214
298	2.255
300	2.271
400	3.107
500	3.97
600	4.87
700	5.82
800	6.81
900	7.86

This equation indicates the relation among the thermal conductivity, the electrical resistivity and the temperatures and will be used in following analysis.

4.2 Current in a Straight Wire

4.2.1 A Straight Wire of Gold

Before we explore the micro-contact problem which is a three-dimensional problem, we discuss the problem in a one-dimensional straight wire of gold shown in Fig 4.3. Its length is $2 \times L$, area is A, the boundary conditions are

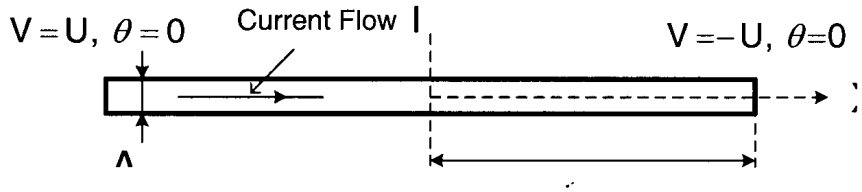

Figure 4.3: A straight wire of gold

$$\begin{aligned} V = U, \quad & \theta = 0, \quad && x = L, \\ V = -U, \quad & \theta = 0, \quad && x = -L. \end{aligned} \tag{4.5}$$

The wire is insulated along lateral surfaces. By the Ohm's law the current density is

$$j_x = -\sigma \frac{dV}{dx}, \tag{4.6}$$

where the electrical conductivity $\sigma \equiv \frac{1}{\rho}$. So, from conservation of charge,

$$\frac{d\, j_x}{dx} = -\frac{d}{dx}\left(\sigma \frac{dV}{dx}\right) = 0. \tag{4.7}$$

Equation (4.7) indicates that the net electric outflow per unit volume passing through any point within the wire is zero and it holds everywhere in the wire.

The electrical conductivity σ is a function of temperature and as U is increased the Joule heating causes a temperature increase so that σ is not a constant. If we regard σ as a function of V (instead of T) , we can write

$$\psi = \int_0^V \sigma d\eta, \tag{4.8}$$

In Appendix D, it is shown that the temperature can be found in terms of the voltage. The conductivity is then written as

$$\sigma = \frac{U_0\sigma_0(1+\tau)}{\sqrt{U_0^2+U^2-V^2}} - \sigma_0\tau. \tag{4.9}$$

where $U_0^2 \equiv T_0 k_0 \rho_0$ and $\tau = \beta T_0$. Now, the problem transforms to essentially a constant conductivity problem. Then, we have

$$\frac{d\psi}{dx} = \sigma \frac{dV}{dx} = -j_x.$$

We want $\dfrac{d^2\psi}{dx^2} = 0$, so we have

$$\psi = \psi_0 \frac{x}{L}, \tag{4.10}$$

where,

$$\psi_0 = \int_0^U \sigma d\eta. \tag{4.11}$$

We also know that total current $I = \psi_0 \dfrac{A}{L}$, therfore,

$$I = \frac{A}{L}\int_0^U \sigma d\eta. \tag{4.12}$$

If U is very small and we can ignore temperature increasing, then $\int_0^U \sigma d\eta \approx \sigma_0 U$, and

$$I = \frac{A\sigma_0}{L}U.$$

We know resistance $R_0 = \dfrac{L}{A\sigma_0}$, so it converts into

$$I = \frac{U}{R_0},$$

which is the linear expression of Ohm's law where the material properties are constant.

Substitute σ by equation (4.9), we get

$$\begin{aligned} I &= \frac{A}{L}\sigma_0 U_0(1+\tau)\int_0^U \frac{d\eta}{\sqrt{U_0^2+U^2-\eta^2}} - \frac{A}{L}\sigma_0\tau U \\ &= \frac{A}{L}\sigma_0 U_0\left[(1+\tau)\arctan\frac{U}{U_0} - \tau\frac{U}{U_0}\right]. \end{aligned} \tag{4.13}$$

A reference constant I_0 is defined by $I_0 = \frac{A}{L}\sigma_0 U_0$, and then,

$$\frac{I}{I_0} = (1+\tau)\arctan\frac{U}{U_0} - \tau\frac{U}{U_0}. \tag{4.14}$$

4.2.2 Analysis and Discussion

The values of the parameters in the equation (4.14) are shown in the Table 4.3. The straight line in Figure 4.4 represents the current-voltage relation when the electrical conductivity is a constant and obviously the relation between them is linear. However, when the electrical conductivity is temperature dependent the current-voltage relation would not be linear. That is because increasing applied voltage leeds current increasing and the temperature increases due to Joule heating. Since the electrical resistivity ρ increases a lot due to higher temperature, the conductivity decreases leeds the current increasing slower than before and reaching maximum value at the instability point, then decreases slowly until the maximum temperature reaches melting point. At the instability point, the contact maximum temperature $\theta_m = 959\,^\circ\mathrm{C}$ is lower than the melting point of gold ($1064\,^\circ\mathrm{C}$). Current also reaches its maximum value at the instability point. If we keep increasing the current after the instability

point the wire will reach the melting point immediately and melt.

Table 4.3: The parameters of the wire

Parameters	Values	Physical Meanings
A	$7.9 \times 10^{-9}\text{m}^2$	Area
L	0.3m	Length
T_0	298K	Room Temperature
k_0	317W/mK	Thermal Conductivity
ρ_0	$2.25510^{-8}\Omega$m	Electrical Resistivity
τ	0.0596	βT_0

Here, the instability point is similar with the "Necking" point in a uniaxial tensile test. Figure 4.5 is a schematic of a typical load-extension curve for a ductile metal during the tensile test. Onset of non-uniform plastic deformation (Necking) occurs at the "Necking" point where the maximum or ultimate load is carried by the specimen. The relation between current and voltage for a micro-contact system is analogous with load-extension or nominal stress-strain relation in a tensile test. Therefore, we give this point the name "Instability" where the current reaches its maximum value and instability behaviors occur. We will discuss the maximum current at the instability point in detail in next section.

Table 4.4 shows the results of currents and applied voltages at instability point and the melting point. The current at instability point is smaller than that at melting point when applied voltage goes higher. In next section we will discuss the same problem when current pass through a micro-contact spot.

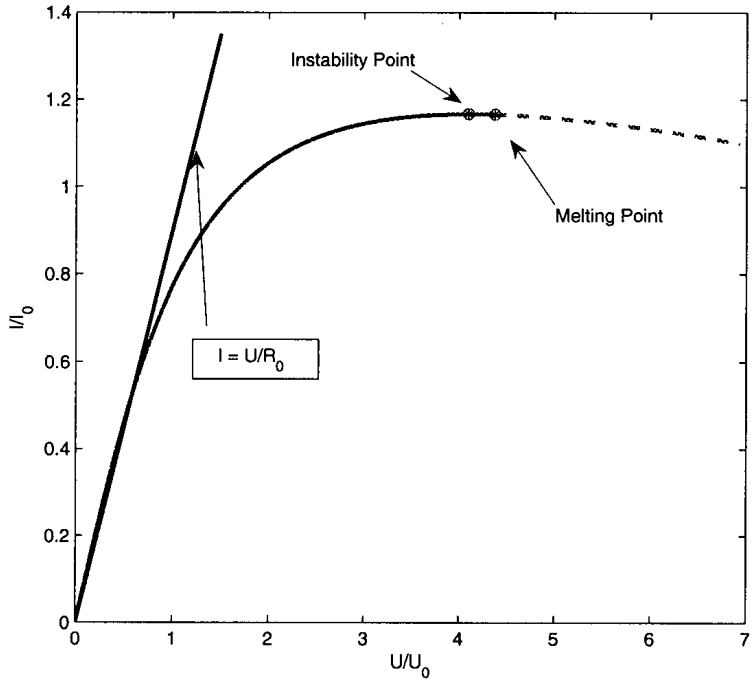

Figure 4.4: Theoretical relation between current and voltage for a straight wire of gold

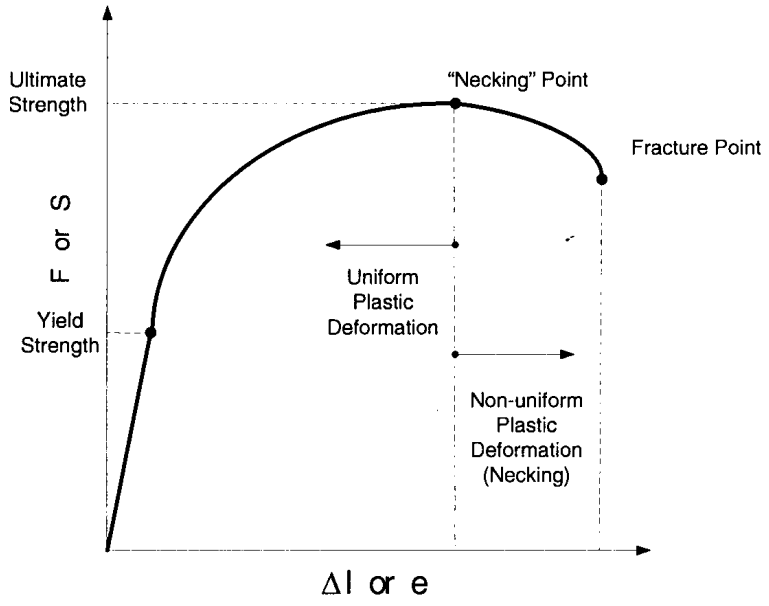

Figure 4.5: Load-extension or nominal stress-strain plot for a ductile metal during a tensile test

Table 4.4: Calculation results of the gold wire

Temperature [°C]	Current I [A]	Applied Voltage U [V]
959(Instability)	1.958	0.189
1064(Melting)	1.956	0.202

4.3 The Current Passing Through the Micro-Contact Spot

4.3.1 The General Problem

Figure 4.6 shows a model of a spot micro-contact system, which is rotationally symmetric with respect to z-axis. The micro-contact system is made up of two relatively large pieces of metal which contact each other over a very small spot.

The radius of the contact spot is $r = a_0$. When the electrical current passes through the surfaces $S1$, $S2$, which are assumed far from the contact spot, the surface potentials $V1$, $V2$ equal to applied voltage U, $-U$, respectively, and the temperature on the surfaces are room temperature T_0. The surface S is assumed electrically and thermally insulated, so; $\frac{\partial V}{\partial z} = 0$. V and $\frac{\partial V}{\partial z}$ are continuous over the contact spot and $V = 0$ at the contact spot. Our purpose is to determine the values of the potential, the temperature, and the current at all points within the micro-contact system. The boundary conditions are

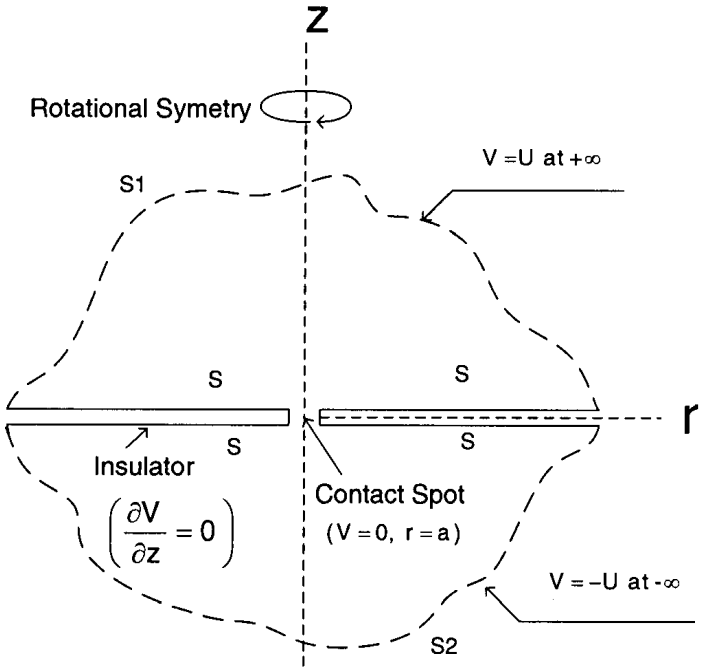

Figure 4.6: Model of a spot micro-contact system

$$
\begin{array}{llll}
V = U & as & r^2 + z^2 \to \infty & z > 0, \\
V = -U & as & r^2 + z^2 \to \infty & z < 0, \\
\dfrac{\partial V}{\partial z} = 0 & & & r > a_0, \\
V \text{ and } \dfrac{\partial V}{\partial z} & \text{are} & \text{continous} & r \leq a_0.
\end{array}
\tag{4.15}
$$

There are three situations for a micro-contact spot,

$$a_0 \gg l,\ a_0 \approx l,\ a_0 \ll l,$$

where the electron mean free path length of gold, $l = 40\text{nm}$. When $a_0 \gg l$, the micro-contact system is a continuum and dominated by Maxwell spreading. We begin to discuss the problem in this situation.

4.3.2 Current-Voltage Relationship

In three dimensional condition, by the Ohm's law the current density can be expressed by,

$$\vec{j} = -\sigma \text{ grad } V, \tag{4.16}$$

so,

$$\text{div } \vec{j} = -\text{ div } (\sigma \text{ grad } V) = 0. \tag{4.17}$$

For this problem we need to define the same function of ψ as we did in last section (see equation (4.8) on page 42), then from equation (4.16) we obtain grad $\psi = \sigma$ grad $V = -\vec{j}$, So,

$$\text{div } \vec{j} = -\nabla^2 \psi = 0,$$

$$\psi = \Omega = \int_0^U \sigma d\eta \qquad as \qquad r^2 + z^2 \to \infty \qquad z > 0,$$
and
$$\psi = -\Omega = \int_0^{-U} \sigma d\eta \quad as \qquad r^2 + z^2 \to \infty \qquad z < 0. \tag{4.18}$$

The electrical flow and temperature across the contact spot continuously. The solution is given on [32].

$$\begin{aligned} \psi &= \Omega \left(1 - \frac{2}{\pi} \int_0^\infty \exp(-\lambda z) J_0(\lambda r) \frac{\sin(\lambda a_0)}{\lambda} d\lambda\right) \qquad z > 0, \\ \psi &= -\Omega \left(1 - \frac{2}{\pi} \int_0^\infty \exp(-\lambda z) J_0(\lambda r) \frac{\sin(\lambda a_0)}{\lambda} d\lambda\right) \qquad z < 0. \end{aligned} \tag{4.19}$$

On the plane $z = 0$, $\psi = 0$ when $r < a_0$, and

$$\frac{\partial \psi}{\partial z} = \frac{2\Omega}{\pi} \int_0^\infty J_0(\lambda r) \sin(\lambda a_0) d\lambda.$$

The current passing through the contact spot

$$I = \int_0^{a_0} 2\pi r \frac{\partial \psi}{\partial z} dr.$$

Since

$$\int_0^{a_0} J_0(\lambda r) r dr = \left[\frac{r}{\lambda} J_1(\lambda r)\right]_0^{a_0} = \frac{a_0}{\lambda} J_1(\lambda a_0),$$

we obtained [33]

$$I = 4\Omega a_0 \int_0^\infty \sin \lambda a_0 J_1(\lambda a_0) \frac{d\lambda}{\lambda} = 4\Omega a_0. \tag{4.20}$$

Substitute Ω by equation (4.18), then,

$$I = 4a_0 \int_0^U \sigma(U, \eta) d\eta. \tag{4.21}$$

If U is very small and we can ignore temperature increasing, then $\int_0^U \sigma d\eta \approx \sigma_0 U$, and

$$I = 4a_0\sigma_0 U.$$

So the constriction resistance $R_0 = \dfrac{1}{4a_0\sigma_0}$ for top portion which is well known relation for the constriction resistance [16].

Substitute σ (see Eq. (4.9) on page 43) in the equation (4.21), then,

$$\begin{aligned} I &= 4a_0\sigma_0 U_0(1+\tau) \int_0^U \frac{d\eta}{\sqrt{U_0^2 + U^2 - \eta^2}} - 4a_0\sigma_0\tau U \\ &= 4a_0\sigma_0 U_0 \left[(1+\tau) \arctan \frac{U}{U_0} - \tau \frac{U}{U_0} \right]. \end{aligned} \tag{4.22}$$

This relation between the current and the applied voltage is a general characteristic for all micro-contacts in the system, and it indicates clearly the breakdown of steady conditions which we discuss in next subsection.

Since the constriction resistance $R_0 = \dfrac{1}{2a_0\sigma_0}$, if we define a dimensionless current and a dimensionless voltage as

$$I_* = \frac{IR_0}{2U_0}, \qquad \text{and} \qquad U_* = \frac{U}{U_0}$$

respectively, then the equation (4.22) can be written

$$I_* = (1+\tau) \arctan U_* - \tau U_*, \tag{4.23}$$

which is shown elsewhere [26].

4.3.3 Analysis and Discussion

From equation (D.4) and equation (D.5) on page 76, since $V = 0$ at the contact spot, the maximum supertemperature θ_m occurs precisely at the contact spot and it is dependent on the applied voltage U, thermal conductivity k_0 and electrical resistivity ρ_0 of the medium at room temperature T_0 instead of the size of the micro-contact spot. If we transfer U and θ_m to the dimensionless voltage $U_* = \frac{U}{U_0}$ and a dimensionless supertemperature $\theta_{m*} = \frac{\theta_m}{T_0}$, respectively, the equation (D.4) becomes

$$U_*{}^2 = 2\theta_{m*} + \theta_{m*}{}^2. \tag{4.24}$$

Figure 4.7 shows the theoretical relation of θ_{m*} versus U_*. In real condition the curve should stop at the melting point of Gold (1064 °C) since there is no steady value possible above this temperature.

Figure 4.8 shows the theoretical relation between current and voltage for the micro-contact system of gold where $\tau = \beta T_0 = 0.0596$. This relation can be implemented by applying a voltage across the micro-contact system form a low impedance source and keeping increasing the voltage [26].

A low impedance source also is called a voltage source which is a circuit component that supplies a fixed potential difference across its terminals that is almost completely independent of the current it supplies. The internal impedance of such a device is very low. Conversely, a high impedance source is called a current source which supply constant current irrespective of the voltage needed by the load across its terminals. The voltage across an ideal current source is completely determined by the circuit connected to the source [27].

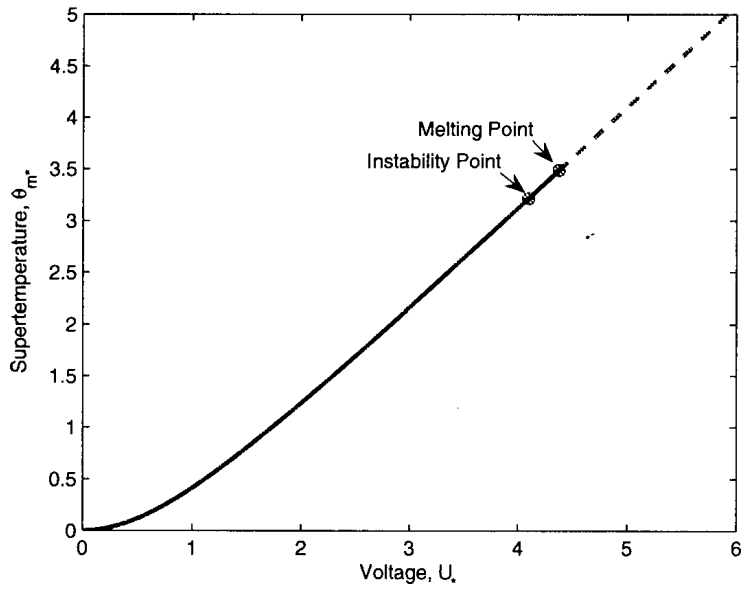

Figure 4.7: Theoretical relation between supertemperature and voltage for a micro-contact system of gold

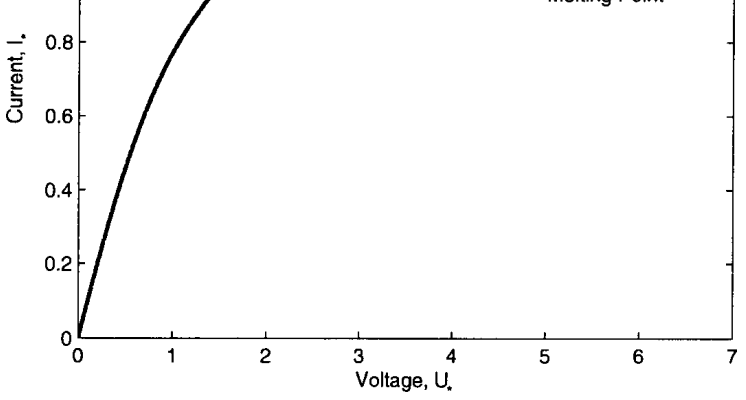

Figure 4.8: Theoretical relation between current and voltage for a micro-contact system of gold

At the beginning stage, since the temperature was low and the electrical resistivity ρ did not change too much comparing with the electrical resistivity at room temperature ρ_0 (Fig 4.2 on page 40), the relation between current and voltage is approximately linear. Further, increasing applied voltage led current increasing and the temperature increased due to Joule heating. Since the electrical resistivity ρ increased a lot due to higher temperature, the current increased slower than before and reached maximum value at the instability point, then decreased slowly until the maximum temperature reached melting point. At the instability point, the contact maximum temperature $\theta_m = 959\,°\text{C}$ is lower than the melting point of gold (1064 °C). Set the radius of the micro-contact spot $a_0 = 80\text{nm}$ which is much bigger than $l = 40\text{nm}$, then we can find out the values of the current (see Table 4.5) at instability point and melting point by using $I_* = \frac{IR_0}{2U_0}$, where, $R_0 = \frac{1}{2a_0\sigma_0}$. They are 764mA and 763mA. Comparing with the results of the straight wire of gold (Table 4.4 on page 47), the values of applied voltage and maximum temperature at two points are same, which indicates the applied voltage and maximum temperature are independent of the size and shape of contact spot. However, the values of current passing through contact spot are different and size-dependent which is expected since the resistances are different for the contact spots with different sizes.

Table 4.5: Calculation results of the micro-contact system

Temperature [°C]	Current I [mA]	Applied Voltage U [V]
959(Instability)	764	0.189
1064(Melting)	763	0.202

Figure 4.9 indicates that, after the instability point, as the current was

decreasing, the maximum temperature kept increasing until it reached melting point. If the micro-contact system is connected into a high impedance circuit

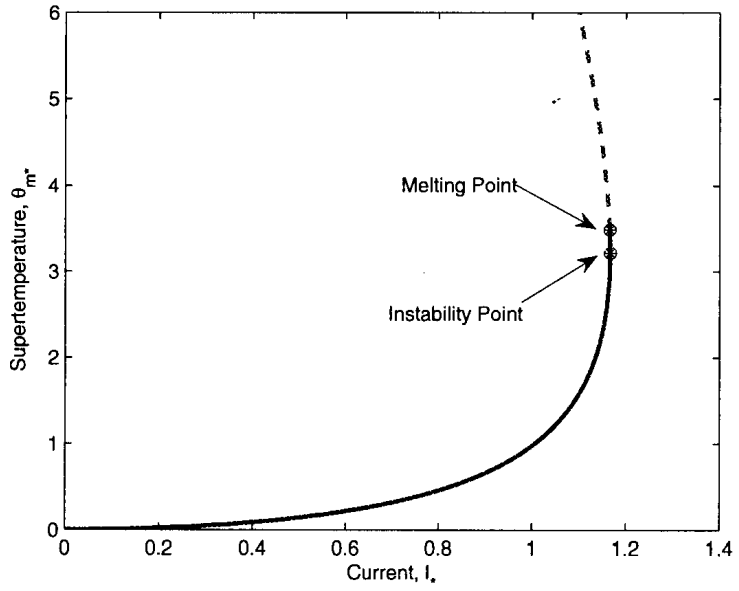

Figure 4.9: Theoretical relation between superatemperature and current for a micro-contact system of gold

where the current is slowly increased and the potential difference is observed, the curve would interrupt at instability point [26]. The contact system was collapsed when the current kept increasing after instability point even though the maximum temperature at the contact spot did not reach the melting point of gold. This can be used to explained the reason that, in the study [24], the contact region collapsed when the temperature is below the melting point of gold.

At different room temperatures, the maximum currents and applied voltages are different at the instability point (see Figure 4.10). At the lower room temperature, applied voltage at instability point is higher and the maximum current is higher too. Further, it needs much higher applied voltage for maxi-

mum temperature reaching the melting point.

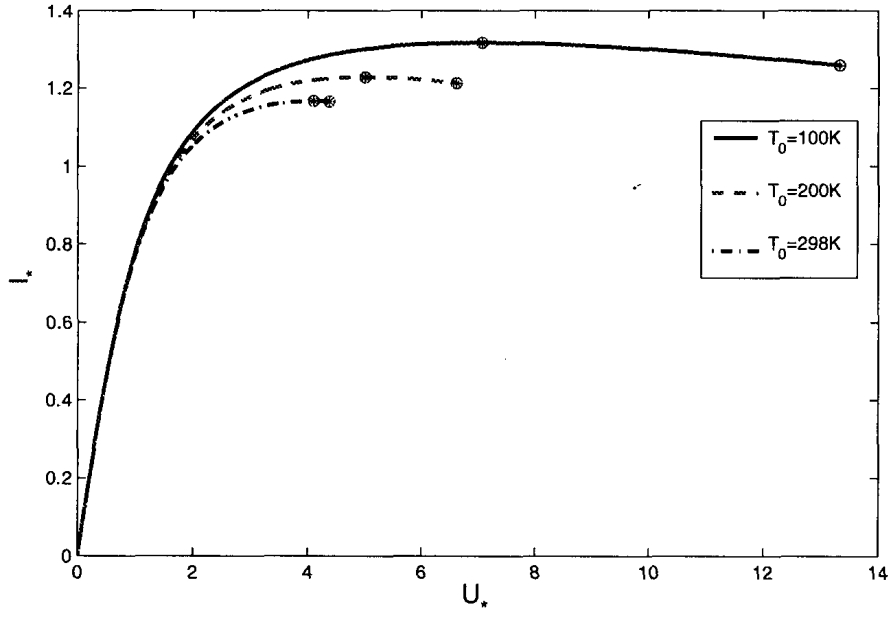

Figure 4.10: Theoretical relations between Current and voltage at different room temperatures

However, when $a_0 \approx l$, or $a_0 \ll l$, we can not use the procedures described above since it is not a continuum any more and dominated by the Sharvin mechanism.

4.4 Heat Generation in Micro-Switch Interfaces

For most of MEMS devices, due to relatively light contact loads, the ratio of real contact area and apparent contact area is between 10^{-4} and 10^{-2} . As mentioned in Chapter 3, even for largest surface interference, Δ_L, all the micro-contact spots radii are smaller than the electron mean free path of gold. Therefore, it is obvious that the constriction resistance in such small micro-

contacts is dominated by the Sharvin mechanism in which electrons travel through the micro-contact ballistically without undergoing any scattering [21].

Since in the Sharvin mechanism electrons travel through the micro-contact ballistically without any interaction or collision with lattices, this resistance component does not lead to any heat generation within the micro-contact system. The resistance contributing to Joule heating is just Maxwell spreading resistance in which electrons travel through diffusively. Therefore, the measured resistance from micro-switch interfaces can not be used to calculate the contact heating because of the existence of the Sharvin resistance.

When $a_0 \gg l$, Utilizing the procedures described in this Chapter we can easily find out the relationships between maximum temperature and applied voltage, maximum temperature and current. The maximum supertemperature θ_m occurs precisely at the contact spot and it is dependent on the applied voltage U, and material properties instead of the size of the micro-contact spot (see equation (4.24)).

Chapter 5

Conclusions

A theoretical study on interfacial temperatures generated at micro-switch contact interfaces has been developed. In addition, surface topography, contact modeling, and electrical contact resistance are described in detail.

A normal contact analysis of two rough gold surfaces characterized by three dimensional fractal geometry was presented. Random rough surfaces were generated from the developed fractal model. The significance of the fractal roughness G and the fractal dimension D on the total contact load and real contact area were discussed in detail. For fixed contact load, decreasing the fractal roughness G or increasing the fractal dimension D increases the real contact area significantly.The biggest truncated area, a'_L is a big portion of total truncated area, A' (from 0.427 to 0.558). Therefore, the calculation of a'_L is critical for the analysis of surface contact.

Electrical contact resistance (ECR) is caused by the roughness of contact surfaces. The constriction resistance of a particular contact asperity is composed of the Maxwell resistance or the Sharvin resistance or both of them, depending on the ratio of the electron mean free path length, l, and the radius

of the asperity, a_0.

Comparing the results of the straight wire of gold and the micro-contact spot ($a_0 \gg l$), the values of applied voltage and maximum temperature at instability point and melting point are same, which indicates the applied voltage and maximum temperature are independent of the size and shape of contact spot. However, the values of current passing through contact spot are different and size-dependent which is expected since electrical resistances are different for the contact spots with different sizes.

If the micro-contact system was connected into a high impedance circuit, it would be melted when the current kept increasing after instability point even though the maximum temperature at the contact spot did not reach the melting point of gold. However, in a low impedance circuit, current reached its maximum value at instability point and decreased slowly until the maximum temperature reached melting point.

Measured resistance from micro-switch interfaces where $a_0 \approx l$, or $a_0 \ll l$ can not be used to calculate the contact heating because of the existence of the Sharvin resistance which does not lead to any heat generation within the interfaces.

Temperature and heat generation analysis in micro-contact system are challenging. The accuracy of this study on it need more demonstrations of future works, especially that of practical experiment. At the same time, this study provides a wonderful reference to future studies since it combines the classical voltage-temperature theory to current heat generation analysis of micro-switches very well.

Appendix A

Surface Generation Programme (Fortran)

```
!main program


INTEGER, PARAMETER  :: N = 1000
REAL,DIMENSION(N+1,N+1)::A
REAL,DIMENSION((N+1)**2) ::B
INTEGER i,j,ii,iii
REAL x,y


!ANALYZING THE DATA

 REAL D
 INTEGER jj,jjj
 INTEGER,DIMENSION(0:10) :: NUM

 REAL,DIMENSION(0:10) ::delt,Ar

!!!!!!!!!!!!!! NUM__ truncated number,Ar__(num/N**2)truncated ratio
```

```
 OPEN (3, FILE='OUT3.TXT')

do 10 i=1,N
   do 20 j=1,N

        x=i*1.0e-9
        y=j*1.0e-9


            WRITE (3, '(F10.9,8X,F10.9,8X,F15.13  )')  x,y ,z(x,y)


          A(i,j)=z(x,y)


 B(ii)=INT(A(i,j)*1.0e13)


 ii=ii+1

   20 CONTINUE
10 CONTINUE


!!!!!!!!!!!!!!!!!!!!!!!!!!!!!!!!!! quick sort now
CALL Quick_Sort( B, 1, (N+1)**2 )

PRINT *, "After: "
!PRINT *, B

PRINT 11, B
 11 FORMAT(9F9.0)

!!!!!!!!!!!!!!!!!!!!!!!!!!!!!!!!ANALYZING THE DATA


D=B((N+1)**2)-B(1)   !B((N+1)**2)=Bmax, B(1)=Bmin
DD=D/Nd
BB=B(1)+DD
```

```
id=1

 do  1000  jd=1 , Nd

            NC(jd)=0


         do while (B(id)<BB) !DO begin

                   NC(jd)=NC(jd)+1

                 id=id+1


         END DO

     BB=BB+DD

       PRINT*,NC(jd)

  1000 CONTINUE

!!!!!!!!!!!!!!!!!!!!!!!!!!!!!!!!!!!!!!!!!!!!!!!!!!! SUBROUTINE Quick_Sort

CONTAINS
  RECURSIVE SUBROUTINE Quick_Sort( X, L, R )
    REAL, DIMENSION(:), INTENT(INOUT) :: X    ! list
    INTEGER, INTENT(IN)               :: L, R ! left, right bounds
    INTEGER L1, R1                            ! etc

    IF (L < R)THEN
      L1 = L
      R1 = R

      DO
        DO WHILE (L1 < R .and. X(L1) <= X(L))  ! shift L1 right
          L1 = L1 + 1
        END DO

        DO WHILE (L < R1 .and. X(R1) >= X(L))  ! shift R1 left
```

```
          R1 = R1 - 1
        END DO

        IF (L1 < R1) CALL Swop( X(L1), X(R1) ) ! swop
        IF (L1 >= R1) EXIT                     ! crossover -
                                               ! partition
      END DO

      CALL Swop( X(L), X(R1) )      ! partition with X(L) at R1
      CALL Quick_Sort( X, L, R1-1 ) ! now attack left subproblem
      CALL Quick_Sort( X, R1+1, R ) ! don't forget right subproblem
    END IF
  END SUBROUTINE Quick_Sort

  SUBROUTINE Swop( A, B )
    REAL, INTENT(INOUT) :: A, B
    REAL                :: Temp

    Temp = A
    A = B
    B = Temp

  END SUBROUTINE Swop

END

!!!!!!!!!!!!!!!!!!!!!!!!!!!!!!!!!!!!!!!!!!!!!!!!!!!!!Solve Funtion z(x,y)

Function z(xz,yz)


REAL gama,L,DD,G, Ls,F1,pi,xz,yz,zz,K1,K2,KK ,pointt,k3

INTEGER M,mm,n ,nmax


INTEGER,DIMENSION(1) :: Seed
REAL phi,R

      M = 10
```

```
      gama = 1.5
      DD = 2.3
      G = 0.1D1 / 0.10000000000000D14
      Ls = 0.1D1 / 0.1000000000D10
      pointt = 5.0
      L =pointt*Ls
      pi=4*atan(1.0)

      F1 = L * (G / L) ** (DD - 2.0) * sqrt(log(gama) / M)

      nmax = int(aint(log(pointt) / log(gama)))


  zz=0.0

 do 100, mm=1,M
    do 200,n=0,nmax


!!!!!!!!!!!!!!!!!!!!!!!!!!!!!!!!!!!!
                                      !
CALL RANDOM_SEED(PUT=Seed)            !
                                      !
CALL RANDOM_NUMBER( R )               !  Generate Random Numbers
                                      !
phi=2.0*pi*R                          !
                                      !
CALL RANDOM_SEED(GET=Seed)            !
!!!!!!!!!!!!!!!!!!!!!!!!!!!!!!!!!!!!


    K1 = gama ** ((DD - 3) * n) * F1


      K2 = cos(KK(xz,yz) - pi * mm / M)

         K3 = 0.2D1 * pi * gama ** n * sqrt(xz ** 2 + yz ** 2) / L

            P = K3 * K2 + phi
```

```
              Q = cos(phi) - cos(P)

                   zz=zz+K1*Q


    200       continue
 100     continue

z=zz

END FUNCTION

!!!!!!!!!!!!!!!!!!!!!!!!!!!!!!!!!!!!!!!!!!!!!!!!!!!!!!!!!!!!!!!!!!!!!!

!!!!!!!!!!!!!!!!!!!!!!!!!!!!!!!!!!!
                                  !
REAL FUNCTION  KK(xs,ys)          !
                                  !
   IF (xs <=0.0) THEN             !
                                  !  Solve Function KK(x,y)
         KK=atan(1.0)*2           !
   ELSE                           !
         KK=atan(ys/xs)           !
                                  !
   END IF                         !
   END FUNCTION                   !
                                  !
!!!!!!!!!!!!!!!!!!!!!!!!!!!!!!!!!!!
```

Appendix B

Load and Resistance Analysis (Maple)

```
#read"c:/program files/maple 9/maplefiles/total resis-load.txt";


gama:=1.5;
DD:=2.44;                              # fractal dimension
G:=9.46*10^(-13);                      # fractal roughness
as_prime:=evalf(Pi)*(10^(-9)/2)^2;  # smallest trucated area
lambda:=40*10^(-9);      # the average electron mean free path (of gold)
rho:=2.3*10^(-8);        # electrical resistivity of gold at room temp.

V:=10;                   # applied votage



Aa:= 10^(-12);                                  # apparent contact area
E:= 80*10^9;                                    # elastic modulus of gold
nu:= 0.44;                                      # Poisson's retio of gold
#Estar:= ((1-nu1^2)/E1+(1-nu2^2)/E2)^(-1);# effective elastic modulus
Estar:= (2*((1-nu^2)/E))^(-1);                  # effective elastic modulus
                                                   # of gold
sigmaY:= 0.53*10^9;                             # the yield strength of the
                                                   # deformable medium of gold
```

```
 A:=array(1..11);              # total real contact area
 F:=array(1..11);              # total load on the surfaces
Rt:=array(1..11);              # total contact resistance


   Delta:=array(1..11);        #surface interference
 A_prime:=array(1..11);        #total truncated contact area
al_prime:=array(1..11);        #biggest truncated contact area
    Numt:=array(1..11);        #total truncated points

##############################

#reading data from "input11 file"

data:=ImportMatrix("c:
       /program files/maple 9/maplefiles/input/input11.txt"):

   Delta:=data[1..11,1]:


   A_prime :=data[1..11,2]:


   al_prime :=data[1..11,3]:


   Numt :=data[1..11,4]:

##############################

fd := fopen("c:/program files/maple 9
       /maplefiles/output/out4.txt", WRITE,TEXT):

for i from 1 to 11 do
```

```
NN:=Numt[i];


ai_prime:=array(1..NN);  # truncated contact area of particular point
ri_prime:=array(1..NN);  # the radius of ai_prime.
  deltai:=array(1..NN);  # the interference distance of particular point
     ai :=array(1..NN);  # real contact area of particular point
     Fmi:=array(1..NN);  # mean contact pressure
     Fri:=array(1..NN);  # load on particular point, Fri:=Fmi*ai
     str:=array(1..NN);  # the representative strain of particular point
      ri:=array(1..NN);  # the radius of ai
      Rc:=array(1..NN);  # the resistance of particular point
     Rcc:=array(1..NN);

##############################

# Contact Deformation model (Calculate ai_prime, ai and Pmi)

 a_prime:=al_prime[i]/N^(2/(DD-1));
 a_prime:=unapply(a_prime,N);


#Calculating

 #A _ total real contact area
 #F _ total contact load
 #Rt_ total contact resistance


  AA:=0;
  FF:=0;
 Rtt:=0;


for j from 1 to NN do

 Nacc:=j:
 ai_prime[j]:=a_prime(Nacc):

  ri_prime[j] :=evalf(sqrt(ai_prime[j]/Pi));
```

```
  deltai[j] := 2*G^(DD-2)*sqrt(ln(gama))
               *(2*ri_prime[j])^(3-DD);
  str[j] :=  Estar*deltai[j]/(sigmaY*ri_prime[j]);



# elastic deformation

  if str[j] < 1.78 then ai[j]:= ai_prime[j]/2;
                Fmi[j]:=(4*sqrt(2)/(3*Pi))*str[j]*sigmaY;

# elastic-plastic deformation

     elif str[j] < 21 then
          ai[j]:= ai_prime[j]/(0.05*(ln(str[j]))^2
                  -0.57*ln(str[j])+2.41);
          Fmi[j]:=(0.70*ln(str[j])+0.66)*sigmaY;

# fully plastic deformation

        elif str[j] <= 400 then
             ai[j]:= ai_prime[j]/(0.05*(ln(str[j]))^2
                     -0.57*ln(str[j])+2.41);
             Fmi[j]:=2.9*sigmaY;

# fully plastic deformation

            else ai[j]:= ai_prime[j]/0.71;
                 Fmi[j]:=2.9*sigmaY;



end if;


############################

#Resistance analysis

ri[j]:=evalf(sqrt(ai[j]/Pi));
```

```
INTT:= Integrate(exp(-x*lambda/ri[j])*sin(Pi*x)/(Pi*x),
                 x=0..infinity):

#comments: INTT= arctan(ri*Pi/lambda)/Pi

  #Rc[j]:= 4*lambda*(rho1+rho2)/(9*ai[j])
              + INTT*(rho1+rho2)/(2*Pi*ri[j]);

  Rc[j]:= 4*lambda*rho/(3*Pi*(ri[j])^2) + 0.694*rho/(2*ri[j]);


      Rcc[j]:=1/Rc[j];
      Rtt:=Rcc[j]+Rtt;



############################

#load analysis


 Fri[j]:=Fmi[j]*ai[j];

 AA:=ai[j]+AA:
 FF:=Fri[j]+FF:


  end do:



  A[i]:=AA;
  F[i]:=FF;
  Pre[i]:=F[i]/Aa;
  Rt[i]:=1/Rtt;

     Aratio[i]:= A[i]/Aa;
 Fratio[i]:=F[i]/(Aa*Estar);
```

```
fprintf(fd,"% 3.2E\t% 3.2E\t% 3.2E\t% 3.2E\t\n"
        ,Delta[i],A[i],Pre[i],Rt[i]);


##############################

end do:

fclose(fd);
```

Appendix C

Programme to Plot Surface Roughness (Matlab)

```
%%%%%%%%%%%%%%%%%%%%%%%%%%%%%%%%%%%%%%%%%
%  programme to plot surface roughness  %
%                                       %
%  012405                               %
%%%%%%%%%%%%%%%%%%%%%%%%%%%%%%%%%%%%%%%%%

clear all;

load out3.txt
nn=size(out3);
%n: the fractal surface is expressed as a n x n matrix
n=nn(1,1)^0.5;
x1=out3(:,1);
y1=out3(:,2);
z1=out3(:,3);

x1=1e6*x1;
y1=1e6*y1;
%x1 and y1 are now in micro meter
z1=1e9*z1;
%z1 is now in nano meter
```

```
x=reshape(x1,n,n);
y=reshape(y1,n,n);
z=reshape(z1,n,n);

for i=1:1:64
   for j=1:1:3
      map(i,j)=0;
   end;
end;
colormap(map);

%figure(1);
subplot(1,2,1)
meshz(x,y,z)
```

Appendix D

Voltage-Dependent Electrical Conductivity

When an electrical current passes through a resistor, the Joule heating leads to the temperature change. In one dimensional condition, heat flux

$$q_x = -k\frac{d\theta}{dx},$$

where k is the thermal conductivity and θ is the supertemperature, and the ner heat outflow per unit volume,

$$\text{div } q_x = \frac{dP}{Adx},$$

where P is electrical power and Adx is volume. We also know the electrical power generated in the volume

$$dP = (j_x A)^2 \frac{dx}{A\sigma},$$

where $j_x A$ is the current passing through the volume and $\frac{dx}{A\sigma}$ is the resistance of the volume. Substitute $j_x = -\sigma\frac{dV}{dx}$, we have

$$\frac{dP}{Adx} = \sigma\left(\frac{dV}{dx}\right)^2,$$

finally we have

$$\frac{d}{dx}\left(k\frac{d\theta}{dx}\right) = -\sigma\left(\frac{dV}{dx}\right)^2, \tag{D.1}$$

which means that for steady conditions the rate of the heat generation inside any volume must equal to the rate at which the heat is passing through its surface [26].

The Kohlrausch equation (for example, see [16, 26]) indicates the relation between the potential-drop V across the terminal and maximum supertemperature θ_m.

$$V^2 = 2\int_{\theta}^{\theta_m} \rho k d\eta, \tag{D.2}$$

where $\rho \equiv \frac{1}{\sigma}$, and equation (D.2) must satisfy the governing differential equation (D.1). To verify it, we differentiate equation (D.2),

$$2V\frac{dV}{dx} = -2\rho k\frac{d\theta}{dx},$$

then multiply both sides by σ,

$$\sigma V\frac{dV}{dx} = -k\frac{d\theta}{dx},$$

then differentiate,

$$\frac{d}{dx}\left(\sigma V\frac{dV}{dx}\right) = -\frac{d}{dx}\left(k\frac{d\theta}{dx}\right),$$

So,

$$V\frac{d}{dx}\left(\sigma\frac{dV}{dx}\right) + \sigma\left(\frac{dV}{dx}\right)^2 = -\frac{d}{dx}\left(k\frac{d\theta}{dx}\right).$$

From equation (4.7) we know $V\frac{d}{dx}\left(\sigma\frac{dV}{dx}\right) = 0$, then the governing differen-

tial equation (D.1) is satisfied.

To solve equation (4.12) on page 43, we need to know σ as a function of the potential V. Substitute $k\rho = k_0\rho_0(1 + \theta/T_0)$ in equation (D.2), we obtain

$$\begin{aligned} V^2 &= 2k_0\rho_0 \int_{\theta}^{\theta_m} \left(1 + \frac{\eta}{T_0}\right) d\eta \\ &= 2k_0\rho_0 \left[\eta + \frac{\eta^2}{2T_0}\right]_{\theta}^{\theta_m}. \end{aligned} \tag{D.3}$$

Since by the boundary condition (Eq. (4.5)) on page 42, $\theta = 0$, $V = U$, we obtain the relation between applied voltage and maximum supertemperature,

$$U^2 = 2k_0\rho_0 \left[\theta_m + \frac{{\theta_m}^2}{2T_0}\right]. \tag{D.4}$$

Also we can get rid of θ_m, then

$$V^2 = U^2 - 2k_0\rho_0 \left[\theta + \frac{\theta^2}{2T_0}\right]. \tag{D.5}$$

By utilizing equation (4.4), we obtain

$$\theta = -T_0 \left(1 - \frac{k\rho}{k_0\rho_0}\right), \tag{D.6}$$

then $\theta + \dfrac{\theta^2}{2T_0}$ can be transformed to $-\dfrac{T_0}{2}\left[1 - \left(\dfrac{k\rho}{k_0\rho_0}\right)^2\right]$, so,

$$V^2 = U^2 + T_0k_0\rho_0 \left[1 - \left(\frac{k\rho}{k_0\rho_0}\right)^2\right].$$

If we define $U_0^2 \equiv T_0k_0\rho_0$, then,

$$\frac{k\rho}{k_0\rho_0} = \frac{\sqrt{U_0^2 + U^2 - V^2}}{U_0}. \tag{D.7}$$

By utilizing equation (4.1) on page 39 and $\rho \equiv \dfrac{1}{\sigma}$, the equation (D.7) is

transformed to

$$\sigma = \frac{U_0\sigma_0(1-\beta\theta)}{\sqrt{U_0^2+U^2-V^2}}. \tag{D.8}$$

By equation (D.6) and equation (D.7), we get

$$\theta = \frac{T_0\sqrt{U_0^2+U^2-V^2}}{U_0} - T_0.$$

Substitute θ in the equation (D.8) and define $\tau = \beta T_0$, finally we obtain the solution for voltage-dependent electrical conductivity σ

$$\sigma = \frac{U_0\sigma_0(1+\tau)}{\sqrt{U_0^2+U^2-V^2}} - \sigma_0\tau. \tag{D.9}$$

Appendix E

Curves of Temperature Analysis (Matlab)

```
%temperature vs. Voltage

 x=0:0.001:3.487;
 %subplot(3,1,1)
     plot(test(x),x,'-','Color','blue','LineWidth',2)
     hold on
   x=3.487:0.01:5;
     plot(test(x),x,'--','Color','red','LineWidth',2)
  plot(4.096,3.216,'o')
   plot(4.096,3.216,'*')
   plot(4.374,3.487,'o')
   plot(4.374,3.487,'*')
 hold off

% Current vs. Voltage
clear

x=0:0.001:3.487;
Us=test(x);
plot(Us,test1(Us),'-','Color','blue','LineWidth',2)
hold on
```

```
x=3.487:0.01:6;
Us=test(x);
plot(Us,test1(Us),'--','Color','red','LineWidth',2)
  plot(4.096,1.167,'o')
  plot(4.096,1.167,'*')
  plot(4.374,1.166,'o')
  plot(4.374,1.166,'*')
hold off

% Temperature vs. Current
clear

x=0:0.001:3.487;
Us=test(x);
plot(test1(Us),x,'-','Color','blue','LineWidth',2)
hold on
x=3.487:0.01:6;
Us=test(x);
plot(test1(Us),x,'--','Color','red','LineWidth',2)
  plot(1.167,3.216,'o')
  plot(1.167,3.216,'*')
  plot(1.166,3.487,'o')
  plot(1.166,3.487,'*')
hold off

%%%%%%%%%%%%%%%%%%%%%%%%%%%%%%%%%%%%%%%%%%%%%%%%%%%%
% function for Is
%function test1=ttt(x)
%gamma=0.0596;
%test1=(1+gamma)*atan(x)-gamma*x;

% Function for Us
%function test=ttt(x)   %test is voltage, x is thetam/T0
%test=sqrt(2*x+x.^2);
%%%%%%%%%%%%%%%%%%%%%%%%%%%%%%%%%%%%%%%%%%%%%%%%%%%%
```

Bibliography

[1] L. Kogut and K. Komvopoulos. Electrical contact resistance theory for conductive rough surfaces. *Journal of Applied Physics*, 94(5), September 1 2003.

[2] Jack W. Judy. Microelectromechanical Systems (MEMS): Fabrication, Design, and Applications. *Journal of Smart Materials and Structures*, 10:1115-1134, 2001.

[3] J. Jason Yao. TOPICAL REVIEW: RF MEMS from a device perspective. *Journal of Micromechanics and Microengineering*, 10(4):R9-R38, December 2000.

[4] S. E. Lyshevski. MEMS and NEMS: systems, devices, and structures. *CRC Press, USA*, 2001.

[5] et al. Ye Wang. A micromachined RF microrelay with electrothermal actuation. *Journal of Sensors and Actuators A*, 103:231-236, 2003.

[6] G.M. Rebeiz and J.B. Muldavin. RF MEMS Switches and Switch Circuits. *IEEE microwave magazine*, December 2001.

[7] et al Paul M. Zavracky. Microswitches and microrelays with a view toward microwave applications. *International Journal of RF and Microwave Computer-Aided Engineering*, 9(4):338-347, 1999.

[8] C. Bozler, R. Drangmeister, S. Duffy, M. Gouker, J. Knecht, L. Kushner, R. Parr, S. Rabe, and L. Travis. MEMS microswitch arrays for reconfigurable distributed microwave components. *IEEE Int. Microwave Symp. Dig.*, pages 153-156, 2000. Boston, MA.

[9] Jeremy A. Walraven. Future challenges for MEMS failure analysis. *Test Conference, 2003. Proceedings. ITC 2003*, 1:850-855, Sep.30-Oct.2 2003.

[10] G.M. Rebeiz. RF MEMS Theory, Design, and Technology. *Wiley Interscience*, 2003. New Jersey.

[11] B.D. Jensen, L.L.-W. Chow, K. Huang, K. Saitou, J.L. Volakis, and K. Kurabayashi. Effect of Nanoscale Heating on Electrical Transport in RF MEMS Switch Contacts. *Journal of Microelectromechanical Systems*, 14(5):935-946, October 2005.

[12] S. Majumder, N. E. McGruer, G. G. Adams, P. M. Zavracky, R. H. Morrison, and J. Krim. Study of contacts in an electrostatically actuated microswitch. *Sens. Actuators A: Phys.*, 93:19-26, 2001.

[13] W. Yan and K. Komvopoulos. Contact analysis of elastic-plastic fractal surfaces. *Journal of Applied Physics*, 84(7):3617, October 1 1998.

[14] K. Komvopoulos and N. Ye. Three-Dimensional Contact Analysis of Elastic-Plastic Layered Media with Fractal Surface Topographies. *Journal of Tribology*, 123:632-640, July 2001.

[15] J. A. Greenwood and J. B. P. Williamson. Contact of Nominally Flat Surfaces. *Proceedings of the Royal Society of London A*, 295(1442):300-319, December 1966.

[16] R. Holm. Electrical Contacts. *Springer, 4th edition, New York*, 1967.

[17] L. Kogut and K. Komvopoulos. The role of surface topography in MEMS switches and relays. *Proceedings of 2004 ASME/STLE International Joint Tribology Conference Long Beach, California USA*, pages 24-27, October 2004.

[18] B. B. Mandelbrot. The Fractal Geometry of Nature. *Freeman, San Francisco, CA*, 1982.

[19] A. Majumdar and B. Bhushan. Fractal Model of Elastic-Plastic Contact Between Rough Surfaces. *Journal of Tribology*, 113:1-11, 1991.

[20] L. Kogut and K. Komvopoulos. Analysis of the spherical indentation cycle for elastic-perfectly plastic solids. *J. Mater. Res.*, 19(12), 2004.

[21] A.G.M. Jiansen, A.P. van Gelder, and P. Wyder. Point contact spectroscopy in metals. *Journal of Physics*, C13:6073-6118, 1980.

[22] N. Agrait. Quantum properties of atomic-sized conductors. *Physics Reports*, 377:81-279, 2003.

[23] G. Wexler. The size effect and the non-local boltzmann transport equation in orifice and disk geometry. *Proceedings of the Physical Society*, 89:927, 1966.

[24] F. P. Bowden and J. B. P. Williamson. Electrical conduction in solids, I. Influence of the Passage of Current on the Contact between Solids. *Proceedings of the Royal Society of London A*, 246(1244):1-12, Jul. 1958.

[25] Seik Oh and Michael D. Bryant. The Transient Temperatore Fields for Two Contacting Bodies Having Different Electric Potentials. *IEEE Transactions on Components, Hybrids, and Manufacturing Technology*, Chmt-9(1), March 1986.

[26] J. A. Greenwood and J. B. P. Williamson. Electrical conduction in solids, II. Theory of temperature-dependent conductors. *Proceedings of the Royal Society of London A*, 246(1244):13-31, Jul. 1958.

[27] Wikipedia. Voltage Source and Current Source—Wlkipedia,The Free Encyclopedia. *http://en.wikipedia.org/*, 2006. Online; accessed 19-April-2006.

[28] A. F. Mills. Heat Transfer. *second edition, Prentice Hall, Inc.*, 1999.

[29] N. H. Frank. Introduction to Electricity and Optics. *second edition, Mcgraw-hill Book Company, Inc.*, 1950.

[30] Beth L. Pruitt, Woo-Tae Park, and Thomas W. Kenny. Measurement system for low force and small displacement contacts. *Journal of Microelectromechanical Systems*, 13(2):220-229, April 2004.

[31] David R. Lide. Handbook of Chemistry and Physics. *Journal of Electrostatics*, pages 11-41, 1996-1997.

[32] H.S. Carslaw and J.C. Jaeger. Conduction of Heat in Solids. *Oxford University Press*, page 216, 1959. Second Edition.

[33] A.P. Prudnikov, Yu.A. Brychkov, and O.I. Marichev. Integrals and Series, Volume 2: Special Functions. *Gordon and Breach Science Publishers, Philadelphia, Pennsylvania, USA*, page 193, 1992.